Medicines for All Institute

Toward Reduced Operating Cost in the Production of Lenacapavir Fragment A: Insights into the Rates of Dynamic Kinetic Resolution as a Function of Temperature, Facilitated by PAT

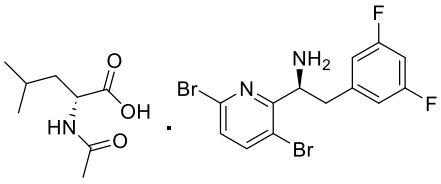

Frag A-NADL
((S)-A1.5-NADL)

Report Prepared by:

Dr. Justina M. Burns
Dr. Limei Jin
Dr. Barrack P. Stubbs
Dr. Roudabeh Moazeni
Carlo Bucci

Contact: m4all@vcu.edu

February 2026

Virginia Commonwealth University
Biotech 8, 737 N. 5th St
Richmond, VA 23219
www.medicines4all.vcu.edu

Executive Summary

This report describes the results of using process analytical technology (PAT) to assess cycle time of the dynamic kinetic resolution (DKR) of *rac*-1-(3,6-dibromopyridin-2-yl)-2-(3,5-difluorophenyl)ethan-1-amine (as its *N*-acetyl-*D*-leucine salt; NADL), as a function of temperature, to form enantiopure *(S)*-Fragment A·NADL. Fragment A, (*S*)-1-(3,6-dibromopyridin-2-yl)-2-(3,5-difluorophenyl)ethan-1-amine, is one of the key starting materials in the synthesis of lenacapavir sodium[1] – a first-in-class, long-acting, HIV treatment and prevention drug developed by Gilead Sciences, Inc. It was approved by the FDA in 2022 for the treatment of HIV (Sunlenca®), in 2025 for prophylaxis (Yeztugo®), and is available for use in both indications.

The purpose of this investigation was to articulate the scope and limitations of conducting the focal point DKR at elevated temperatures, to estimate prospective operating cost savings viz-á-viz faster reaction rates, and to demonstrate an inline, manufacturing-suitable method for monitoring DKR progress. This work was initiated in view of the long DKR cycle time cited by Gilead in their pioneering Fragment A work, its implications for the duration of manufacturing campaigns and, in turn, lenacapavir product costs. PAT was investigated as means to provide real-time measurements for monitoring DKR progress, which results in salt formation of lenacapavir fragment A (**(*S*)-A1.5**). As a non-destructive, inline measurement it provides fast and accurate information of reaction progress, removing the need for manual sampling and long analysis times. For this reaction, inline IR (ReactIR) was used to monitor the reaction progress and builds on work started in Len Frag A PDR (Process Development Report; August 2024).

Medicines for All (M4ALL) has undertaken efforts to further understand and characterize the kinetics of the DKR reaction, leading from the racemic amine to the desired enantiopure isomer. Herein, the goal was to incorporate PAT to optimize the DKR reaction time (i.e., facilitate endpoint identification) and improve throughput. The main analytical method for the experiments revolved around monitoring by FTIR with complementary methods of GC-MS to track reaction

[1] (S)-1-(3,6-dibromopyridin-2-yl)-2-(3,5-difluorophenyl)ethan-1-amine, the free base derived from the enantiopure NADL salt, is used in the convergent synthesis of lenacapavir sodium.

progress. The incumbent process for the basis of this work exhibited 66%-68% isolated yield and 100% chiral purity (enantiomeric excess, ee) (Len Frag A PDR (August 2024)) with a cycle time of 102 hrs (4.25 days) for conversion of **A1.5** to **(*S*)-A1.5-NADL**. The experiments reported here demonstrate the temperature dependance of this process with isolated yield for **(*S*)-A1.5-NADL** ranging from 33%-58% and ee ranging from 67%-100% and cycle times between 20 hrs-98 hrs (0.8 days-4.1 days). Lower yields and lower ee correspond to higher initial temperatures.

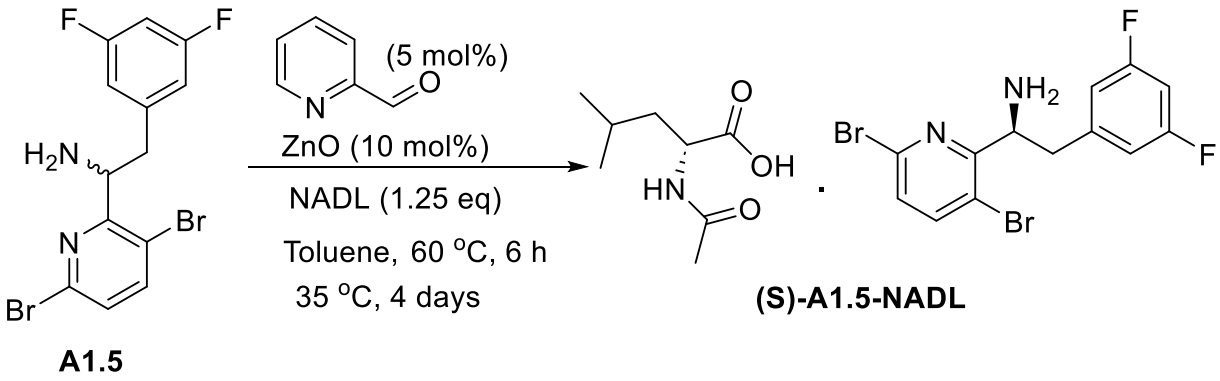

A1.5 **(S)-A1.5-NADL**

Medicines for All – Contributors to the Research and Report

Contributor	Title/Role
Dr. Ryan Littich	Chief Technology Officer
Dr. Justina M. Burns	Assoc Dir of Analytical Chemistry (Project Lead)
Dr. Limei Jin	Assoc Dir of Process Development (Project Lead)
Dr. Roudabeh Moazeni	Process Analytical Scientist II
Dr. Barrack P. Stubbs	Senior Analytical Chemist
Dr. Chiranjeevi Barreddi	Postdoctoral Researcher
Dr. Ramakrishna Sayini	Postdoctoral Researcher
Bradley Ellis	Project Manager
Carlo Bucci	Process Economics Analyst
Saeed Ahmad	Director of Process Economics and Market Intelligence

Contents

1 Introduction

Human immunodeficiency virus (HIV), the virus that causes AIDS (acquired immunodeficiency syndrome), is one of the world's most serious health and development challenges. Approximately 39 million people are currently living with HIV, and tens of millions of people have died of AIDS-related causes since the beginning of the epidemic.[2] In 2020, there were approximately 20 million people on antiretroviral therapy (ART), a number which was expected to reach 24 million by 2024. Approved HIV treatment regimens currently fall into seven drug classes, based on their distinct mechanism of action. Today, approximately 22 million individuals are on a dolutegravir-based regimen: the "gold-standard" treatment comprises the combination of two nucleoside reverse transcriptase inhibitors (NRTIs), tenofovir disoproxil and lamivudine, and the integrase strand transfer inhibitor dolutegravir.[3]

Lenacapavir (Sunlenca®) is a high-potency HIV treatment (available under the tradename Sunlenca®) and prophylactic intervention (available under the tradename Yeztugo®) developed and in development marketed by Gilead Sciences, Inc. The small molecule drug is a first-in-class HIV-1 capsid protein inhibitor that displays picomolar activity, extended pharmacokinetics, and little to no cross-resistance with clinically used antiretroviral agents.[4,5] Lenacapavir achieves its revolutionary anti-HIV-1 activity by blocking the viral replication of the HIV-1 virus, which is closely related to many processes of the viral lifecycle: uptake, assembly, and release.[1] Because of this classification, the FDA has designated lenacapavir as a breakthrough drug. The novel therapy earned approval from both the European Commission and the FDA in 2022 as a treatment for multidrug-resistant HIV (MDR HIV) infections.[6–8] In 2023, in the United States, the cost for HIV-indicated injections and tablets (wholesale; not for PrEP) was $42,450 per patient per year.[9–11] To ensure patient access to lenacapavir-for-PrEP globally, significantly lower annual costs must be realized.[8]

Structurally speaking, lenacapavir is an extremely complex active pharmaceutical ingredient (API), with three chiral sp^3-hybridized carbon centers and 10 fluorine atoms in four

different functional environments. Lenacapavir consists of three advanced intermediates - Fragment A (Frag A), Fragment B, and Fragment C - as shown in **Scheme 1.1**.

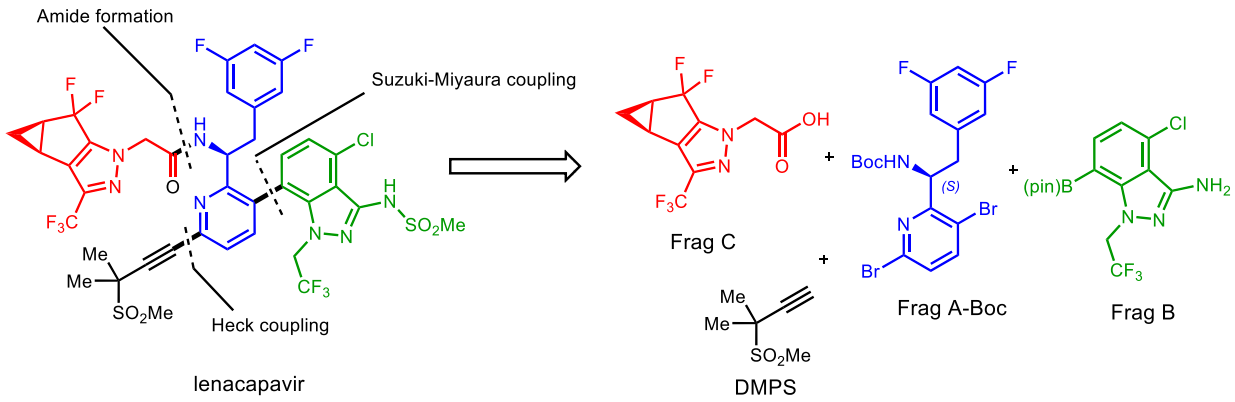

Scheme 1.1. Retrosynthetic disconnections in lenacapavir

Gilead has published several patents related to the initial synthesis and optimization of this molecule with several approaches to each fragment being demonstrated.[12,13,15,16] These routes utilize expensive starting materials and reagents, and rely on costly chiral separation techniques that are not amenable to scaleup.

M4ALL previously developed a DKR-based approach to decrease raw material costs associated with Frag A synthesis (Len Frag A Process Development Report (PDR; (August 2024)).[18] This report focuses on the penultimate step shown in **Scheme 1.2**: the transformation of racemic **A1.5** to the desired S enantiomer, **(*S*)-A1.5**. M4ALL hypothesized that running this step at a higher initial temperature could decrease the cycle time and in turn reduce the operational cost for this step. The strategy proposed by M4ALL was to perform four experiments at varying temperatures, 60°C (baseline), 80°C, 100°C, and 110°C with all reactions occurring on a 5g scale. From this data, the experiment yielding the best result was to be repeated on the same scale to confirm reaction speed and feasibility, after which, the best result was scaled to 20g and monitored.

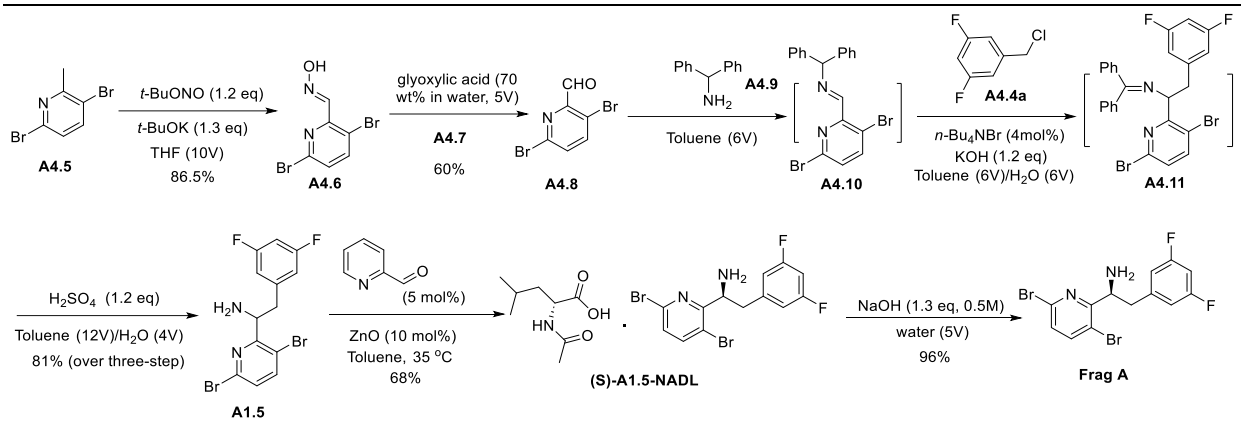

Scheme 1.2. M4All approach for the synthesis of Frag A

2 Results and Discussion

2.1 Methods, Setup, Selection of Process-Indicative IR Resonances

The dynamic kinetic resolution to transform racemic **A1.5** to **(*S*)-A1.5-NADL** was performed in the same manner set forth in Len Frag A PDR (August 2024) with the only variable being the initial temperature set point (**Table 2.1.1**).[18] ReactIR was used for continuous real time monitoring of the reaction, in situ. The reactor setup, incorporating the ReactIR probe, is illustrated in **Figure 2.1.1.** ReactIR setup and calibration details are available in Section 2.4.1.

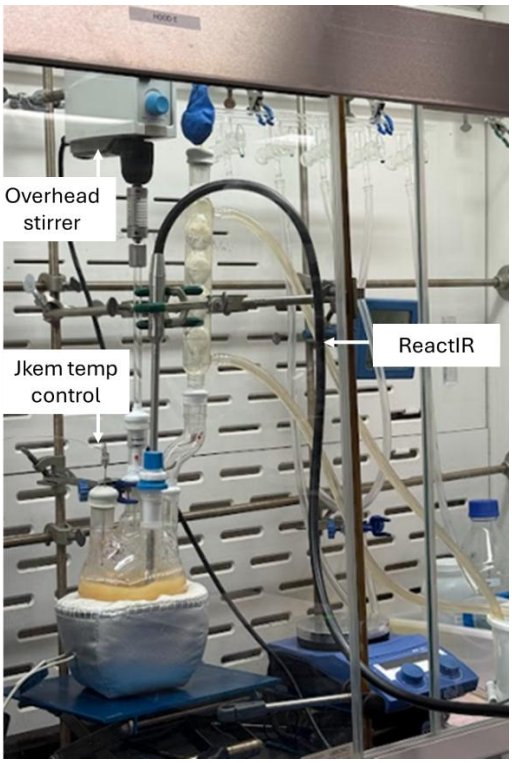

Figure 2.1.1. Image of reaction setup.

M4ALL conditions for dynamic kinetic resolution of **A1.5** to **(*S*)-A1.5-NADL**, reported in Len Frag A PDR (August 2024), included an initial incubation at 60°C for 6 hrs after which the reaction was cooled to 35°C and held until completion (4-10 days).[18] These conditions were repeated in the present work, and are considered the baseline and comparison point for all other tested temperatures. All reactions were performed in toluene on a 5g scale to confirm temperature dependence.[2] The best condition - as determined by optimal reaction time and enantiomeric excess (ee), with absence of new impurities - was repeated at 5g and 20g scales.

All experiments in **Table 2.1.1** utilized PAT to provide real-time measurements for reaction monitoring. ReactIR was used as the primary method for monitoring reaction progress. Solution concentration of **A1.5** and temperature were monitored continuously using the ReactIR

[2] The proposal (GFN-002A Proposal, July 2025) for this work nominated 120°C as a test point. 110.6°C was ultimately the highest temperature assessed, governed by toluene's reflux temperature.

throughout the experiment. **A1.5**'s *in situ* concentration was assessed three ways: 1) peak height (gray) at 820 cm^{-1}; 2) peak area at 825-815 cm^{-1}; and 3) partial least squares (PLS) modeling using the full IR spectra after the IR data were exported.[3] The three methods were statistically tested using the R^2 similarity correlation and generally found that the R^2 regression was >0.9 (See Section 5 Appendix for plots) indicating results are likely to be similar between the three approaches. The exceptions were the 110°C experiment which was performed close to toluene reflux temperature (110.6°C) and the 20g 80°C experiment which had difficulties due to a film forming on the IR probe (See Section 2.2.1 below for further discussion). A representative plot of DKR reaction progress can be found in **Figure 2.1.2** with all others included in the Appendix. The data in these plots represent the concentration of **A1.5** remaining in solution as over the course of the DKR, the desired enantiomer **(*S*)-A1.5** precipitates as its NADL salt. To complement and corroborate ReactIR data, discrete samples were taken and filtered prior to concentration analysis by GC-MS at T = 0 hr, 6 hrs, and final.[4] Dynamic kinetic resolution experiments were deemed complete when the IR concentration was <5 mg/mL in the reaction solution or if no concentration change was observed over six hours (i.e., Δ[**A1.5**] = 0).

For final isolated solids, LC-UV (225 nm) was used to quantify both **(*S*)-A1.5** content and **NADL** content. SFC-UV was used to determine enantiomeric excess (ee), and thermogravimetric analysis (TGA) was performed to quantitate residual toluene as well as any water that may have been absorbed by the isolated material (mitigating **(*S*)-A1.5** hygroscopicity).

[3] With respect to 1) and 2), these IR resonances are unique to racemic **A1.5** in toluene solution. Please see section 4.2.1.1 for additional details, associated IR spectra overlays.

[4] The objective of ReactIR and corroborating GC-MS analyses is to quantify the distribution of species remaining in solution; during the course of the DKR, the desired enantiomer **(*S*)-A1.5** precipitates as its NADL salt.

Table 2.1.1. Experiments performed and total reaction time.

Entry	ELN #	Scale	Initial Temperature[a]	Reaction Time[b]
1	SRK221-X2	5g	60°C for 6 hrs[c]	98
2	BCH219-X3	5g	60°C for 6 hrs[c]	96
3	SRK221-X3	5g	80°C for 6 hrs	44
4	SRK221-X5	5g	80°C for 6 hrs	48
5	BCH219-X6	20g[d]	80°C for 6 hrs	92
6	BCH219-X1	5g	100°C for 6 hrs	20
7	SRK221-X4	5g	100°C for 6 hrs	22
8	BCH219-X2	5g	110°C for 6 hrs	46

[a] After the initial temperature was maintained for 6 hrs, the reaction was cooled and held at 35°C until the reaction was complete. [b] Reaction was considered complete when the IR read <5mg/mL or if Δ[**A1.5**] = 0 for 6 hrs [c] Considered baseline based on Len Frag A PDR (August 2024) [d] 80°C was chosen as the optimum condition based on reaction time and lack of new impurities.

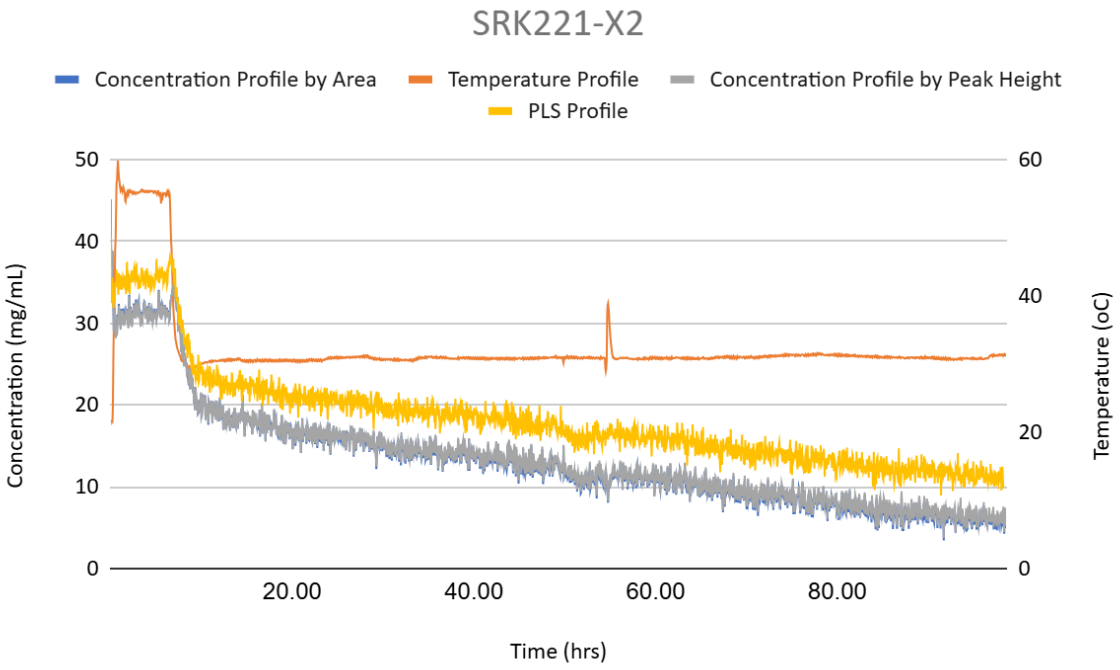

Figure 2.1.2. Representative plot of the soluble form of **A1.5** concentration in toluene over time (IR data) along with the reaction temperature profile for the 60°C temperature. The concentration profile was obtained in three ways: 1) peak height (gray) at 820 cm^{-1}; 2) second peak area at 825-815 cm^{-1} (blue); 3) PLS modeling (yellow) prediction after the IR data exported and modeled using the entire IR spectrum. Orange represents the reaction temperature vs. time as recorded by the IR probe.

2.2 Noteworthy Troubleshooting during PAT Implementation

2.2.1 Disparities between in-situ Concentrations Determined by ReactIR and GC-MS

As noted in Section 2.1 above, the GC-MS was used as a complementary technique to the ReactIR at specific timepoints within the reaction. These timepoints (T = 0 hr, 6 hrs and when Δ[**A1.5**] = 0 or [**A1.5**] = 5 mg/mL by ReactIR) corresponded to the reaction start, the point where the reaction temperature changed to 35°C and immediately prior to the reaction being filtered (i.e. reaction completion). Comparison of the concentrations determined via single IR peak monitoring (820 cm^{-1}), PLS IR spectrum modelling and GC-MS highlighted differences in absolute

concentration but not trend. **Figure 2.2.1.1** shows the comparison between these techniques. It is hypothesized that the concentration differences arise from the build-up of a film on the IR probe as the reaction progressed. Work summarized in Len Frag A PDR (August 2024)[18] showed that the presence of particulates did not impede the ability of the IR probe to measure concentration. However, it was found here that after being submerged in the heterogeneous reaction mixture for extended periods, the probe window was obstructed by gelatinous material which had to be periodically washed away (**Figure 2.2.1.1**). It is hypothesized that when the temperature is cooled to 35°C, a film begins forming on the IR probe. The observed gelatinous material was bulky enough to interfere with the probe and impact data collection. Identification of this material was outside the scope of this work. The effects of this were particularly noticeable for the 20g, 80°C experiment (See Section 5 Appendix). Further investigation of this phenomenon is recommended, as readers prepare to implement this PAT approach – particularly, if the probe cannot be periodically removed for cleaning during the reaction.

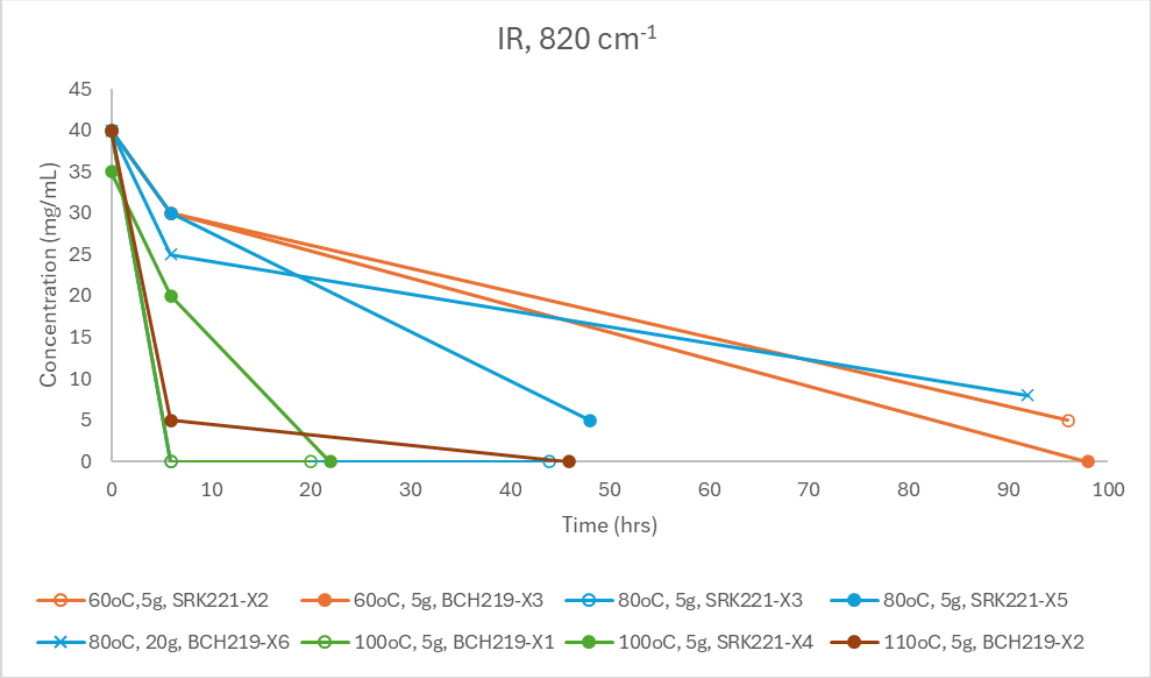

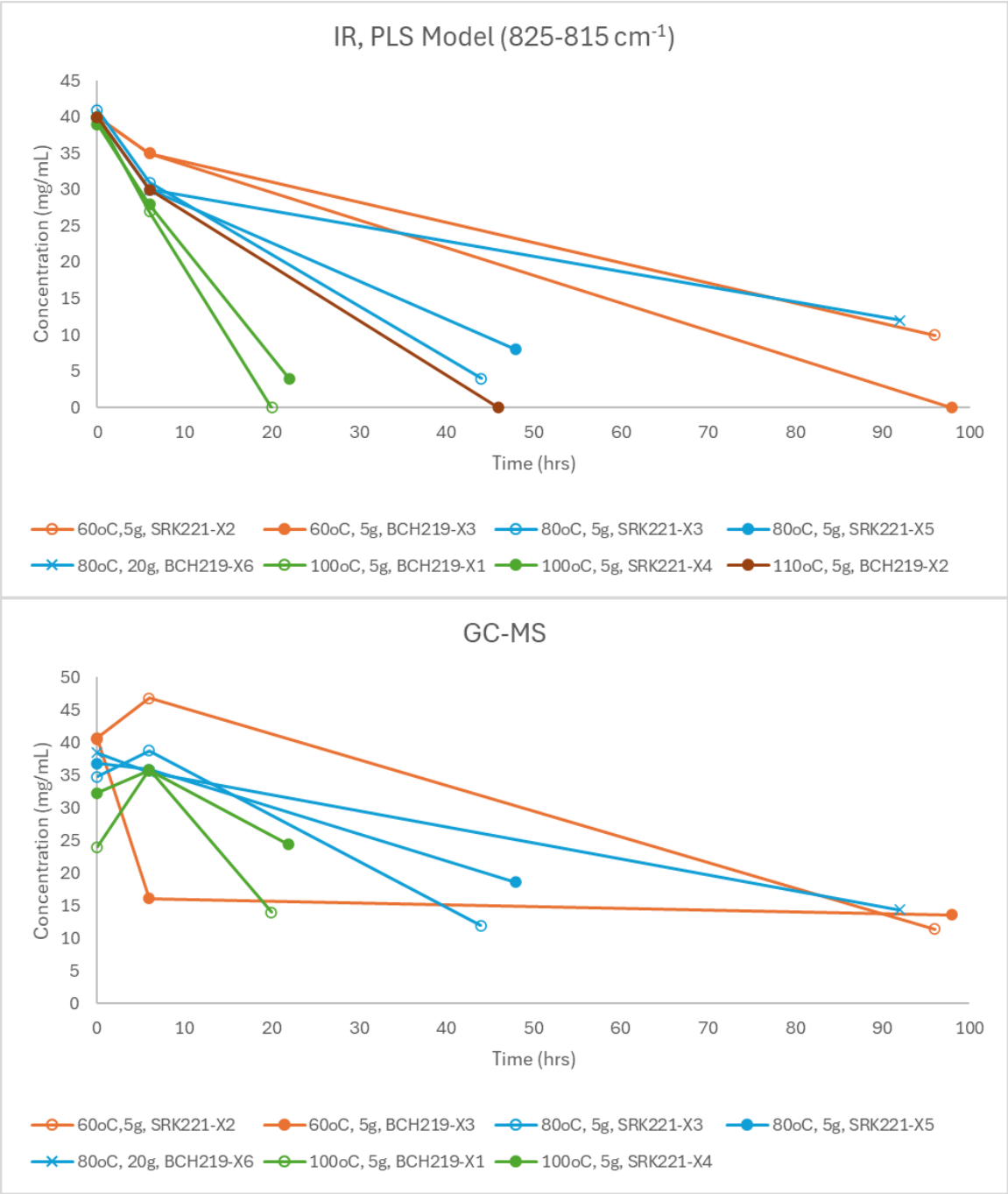

Figure 2.2.1.1. Reaction samples were taken at T = 0 hr, 6 hrs and when Δ[**A1.5**] = 0 or [**A1.5**] = 5 mg/mL by IR and analyzed via GC-MS to determine the concentration of **A1.5**. Samples were filtered prior to GC-MS analysis. While absolute concentrations between the IR (820 cm^{-1} and PLS

model) and GC-MS show differences, the trend is the same across the techniques even though absolute concentrations are not.

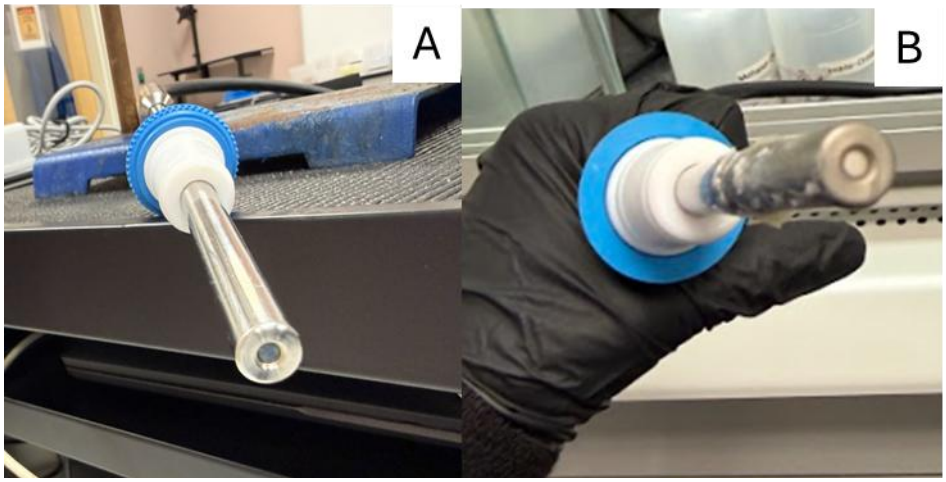

Figure 2.2.1.2. A) Image of clean probe head. B) Image of the gelatinous material covering the IR probe head.

2.2.2 Concentration Spikes in ReactIR Spectra

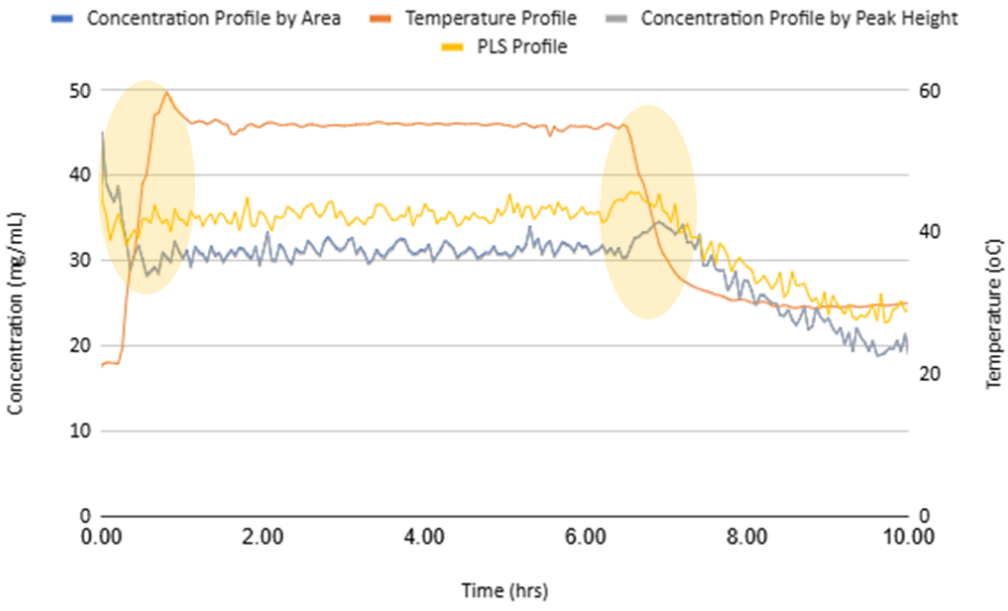

Figure 2.2.2.1. Zoomed in view of SRK221-X2 from **Figure 2.1.2** with concentration increases observed upon temperature change highlighted in yellow.

Short-term concentration increases (i.e., spikes) were observed in ReactIR spectra throughout the variable-temperature investigation of DKR kinetics (**Figure 2.2.2.1**). This phenomenon proved attributable to user-led temperature changes in the reactor. The authors observed that the ReactIR probe requires ~30-45 minutes to re-equilibrate after a temperature change occurs. This was tested separately from these experiments to confirm the hypothesis using a 50 mg/mL standard of **A1.5** (**Figure 2.2.2.2**). **Figure 2.2.2.2** shows that there is ~16% difference in the peak area/height for the standard when the temperature was varied. While this will affect the perceived absolute concentration, it will not affect the trend for monitoring purposes and would not negatively impact the overall endpoint decision particularly if the Δ[**A1.5**] = 0 over 6 hrs.

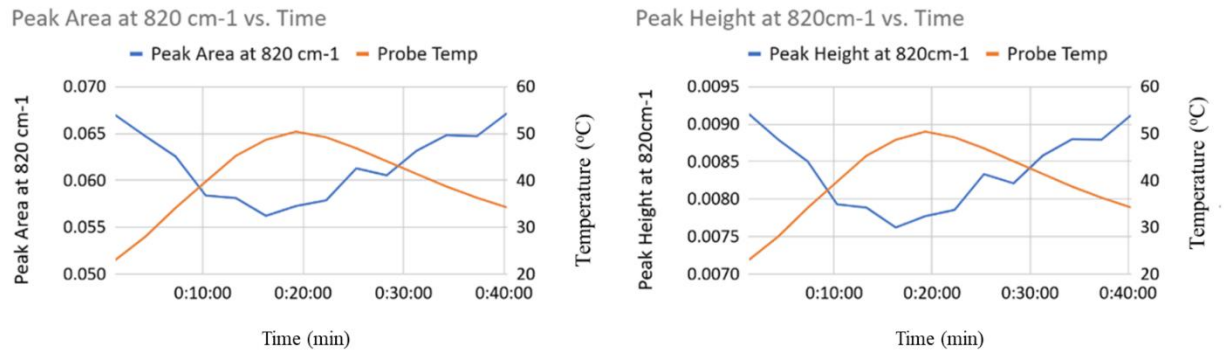

Figure 2.2.2.2. Dependency of IR probe to temperature at selected peak area 820 cm^{-1} utilizing a 50 mg/mL **A1.5** standard. Blue = peak area/height. Orange = IR probe temperature

2.3 Temperature Dependence of Dynamic Kinetic Resolution of **A1.5** to **(*S*)-A1.5-NADL**

Temperature-variable dynamic kinetic resolution experiments revealed tradeoffs between cycle time, conversion to the desired **(*S*)-A1.5-NADL** salt, and its enantiomeric purity. Comparison of these factors across all temperatures led to the following observations and conclusions (**Table 2.3.1**):

- Reaction times decrease with increasing preliminary incubation temperature. This has the potential to positively impact overall cycle time and reduce cost in a manufacturing facility (**Figure 2.3.1**).

  - The 20g scale 80°C reaction required ~2x longer to reach completion compared to the 5g, 80°C reaction. It is hypothesized that the longer reaction time is related to mixing and mass transfer differences between the different size reactors used.[19]
- At temperatures of 100°C and higher, condensation of **A1.5**'s primary amine and the carboxylic acid of **NADL** was observed, resulting in the impurity **A1.5-Amide** (entries 6-8). The identity of the impurity was confirmed via direct synthesis and analysis, per Section 4.3.2. It was further determined that the peak at 13.3 min in the 225 nm LC-UV chromatogram corresponded to the **A1.5-Amide** impurity (**Figure 2.3.2**). Temperatures exceeding 100°C were eliminated from further investigation and are not recommended as means to accelerate the dynamic kinetic resolution of **A1.5** to **(*S*)-A1.5.**
- Enantiomeric excess decreased as the temperature increased, particularly at temperatures exceeding 100°C (**Table 2.3.1, entries 3-5**). However, initial incubation at 80°C for 6 h reliably resulted in high ee for **(*S*)-A1.5** (**Figure 2.3.2**).
- Weight assays decreased with increasing reaction temperature, depressing the isolated yields.
  - Weight assays were performed on the isolated **(*S*)-A1.5-NADL** material which had not been washed with base to convert the material from **(*S*)-A1.5-NADL** to **(*S*)-A1.5** (freebase). As a result, the quantitative amount of **NADL** present exceeds the theoretical (expected 69% **(*S*)-A1.5** and 31% **NADL**); this is attributable to the 0.25 equivalent excess employed in the DKR, relative to **A1.5**. The isolated yield is calculated based on corrected values.

Considering reaction duration, presence/absence of new impurities, enantiomeric purity and purity assayed by weight, it was determined that an initial reaction temperature of 80°C was the best temperature to test at larger scale.

Table 2.3.1. Analytical results and isolated yields for **(*S*)-A1.5-NADL**.

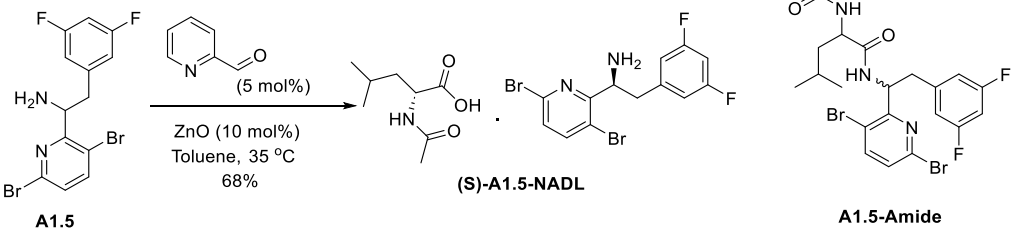

Entry	ELN #	Initial Reaction Temp.	Reaction Time to Achieve Δ[A1.5] = 0)	LC-UV LCAP (%) at 225 nm				LC-UV Wt % at 225 nm[d]		EE by SFC (%)	Isolated Yield (%)
				(*S*)-A1.5	NADL	A1.5-Amide Impurity	Unkwn [c]	(*S*)-A1.5	NADL		
1	SRK221-X2	60°C	98 hr	95.7	4.3	ND[b]	ND[b]	52.1± 0.8	45.9	99.6	54%
2	BCH219-X3		96 hr	95.3	4.7	ND[b]	ND[b]	48.0 ± 1.1	41.6	100	50%
3	SRK221-X3	80°C	44 hr	94.7	5.3	ND[b]	ND[b]	47.6 ± 1.6	52.3	100	49%
4	SRK221-X5		48 hr	92.8	7.2	ND[b]	ND[b]	40.1 ± 2.1	53.1	100	42%
5	BCH219-X6		92 hr[a]	94.6	4.8	ND[b]	0.6	56.1 ± 1.2	44.8	98.8	58%
6	BCH219-X1	100°C	22 hr	89.0	8.9	1.8	0.1	37.9 ± 1.3	61.1	97.6	39%
7	SRK221-X4		20 hr	88.5	9.1	1.6	1.0	31.6 ± 1.3	57.5	95.7	33%
8	BCH219-X2	100°C	46 hr	2.4	5.3	18.8	3.5	39.4 ± 0.7	47.3	67.8	41%
Ref.[e]	n/a[e]	60°C[e]	102 hr[e]	-	-	-	-	76-80[e]	-	100[e]	66%-68%[e]

[a] Performed at a 20g scale. [b] ND = Not detected [c] Retention times = 12.5 min and 13.0 min [d] Purity data presented herein reflect residual NADL, which is typically removed before **(*S*)-A1.5**'s use in the convergent synthesis of lenacapavir sodium. [e] 25g, 60°C from Len Frag A PDR (August 2024)

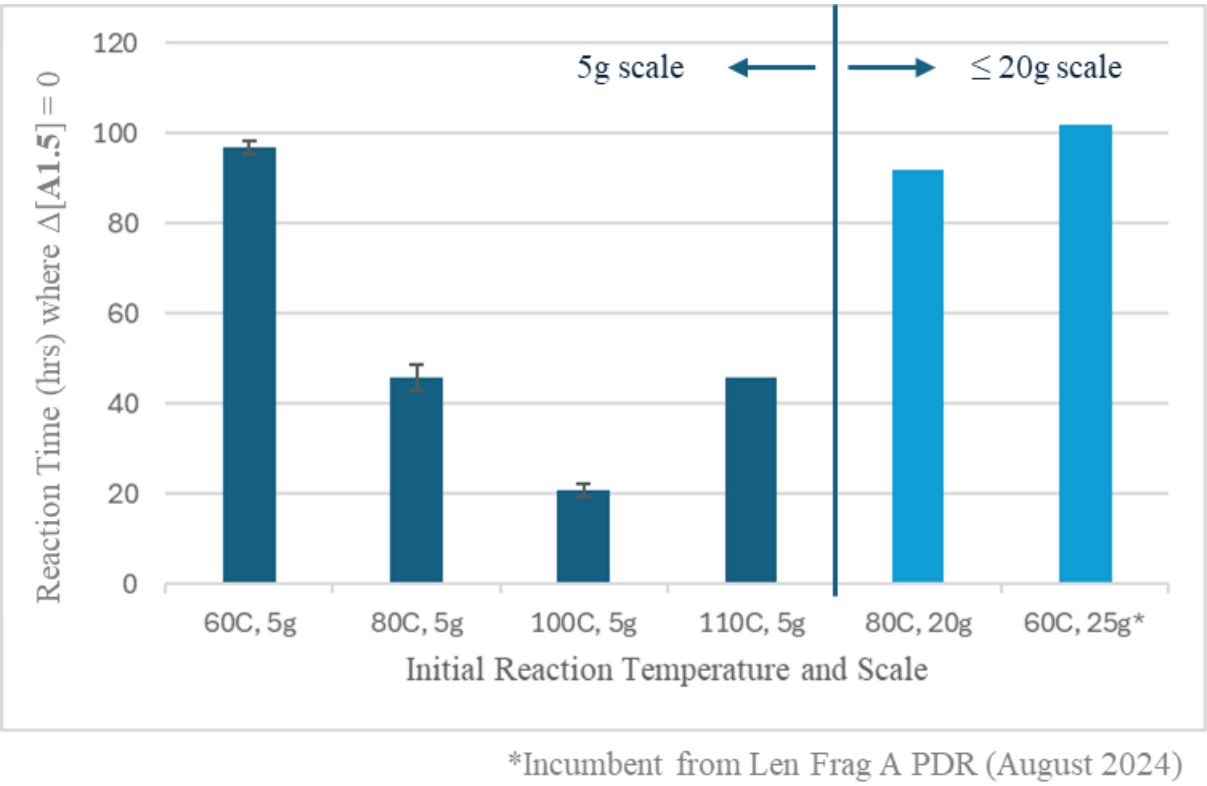

Figure 2.3.1. Reaction time (Δ[**A1.5**] = 0) is inversely related to temperature with longer times observed at larger scales.

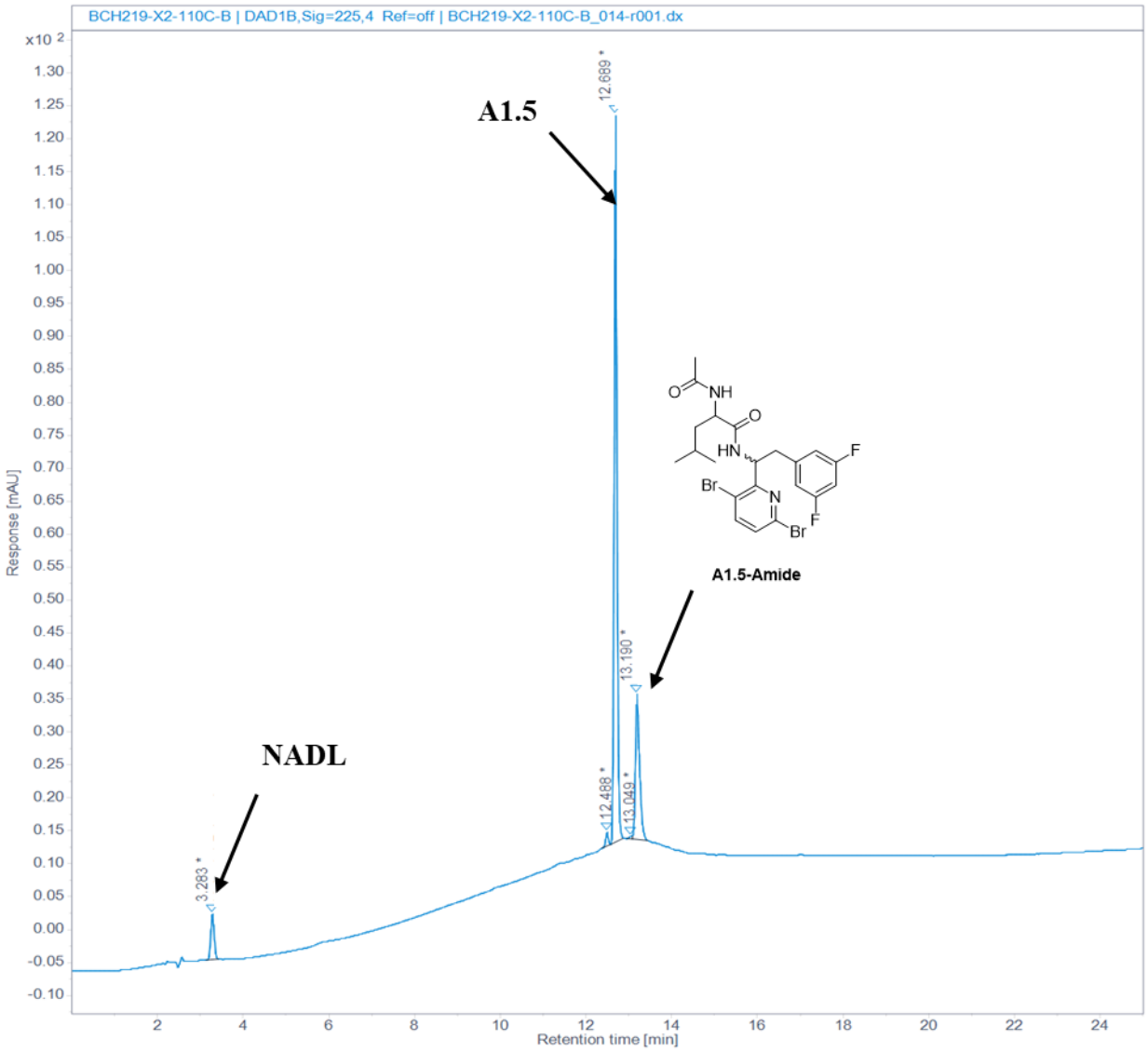

Figure 2.3.1. Representative LC-UV chromatogram for the isolated solid (110ºC, BCH219-X2, 5g) depicting the appearance of new impurities, specifically **A1.5-Amide** at 13.2 min.

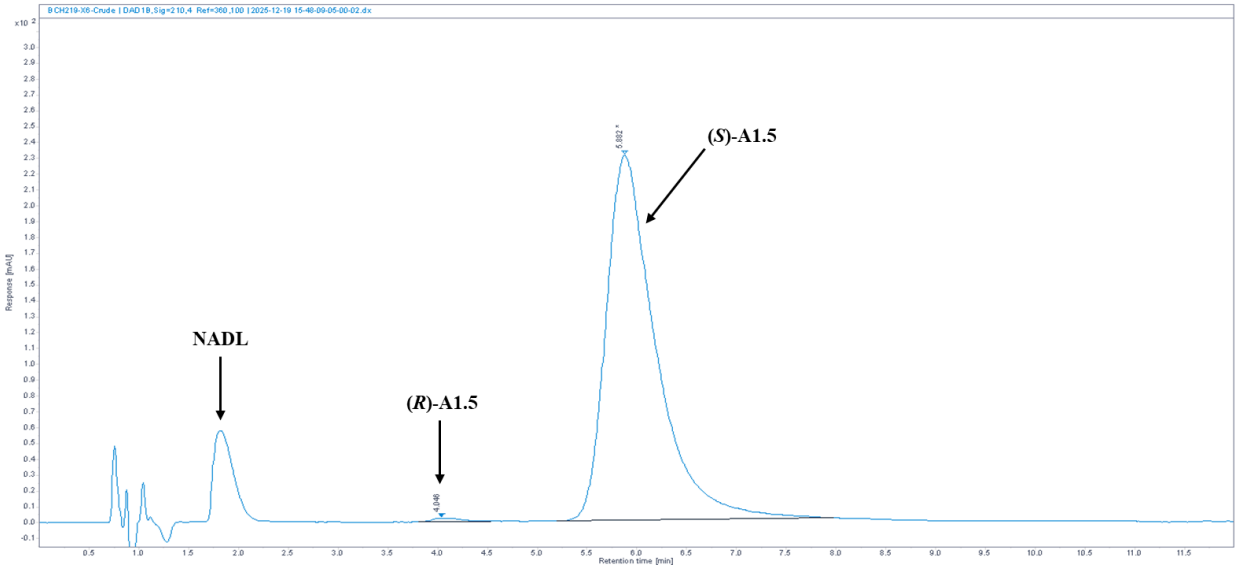

Figure 2.3.2. Representative SFC-UV chromatogram for the isolated solid (80°C, BCH219-X6, 20g). The unintegrated peak ~2 mins is **NADL** (80°C), **(*R*)-A1.5** elutes at ~ 4 min and **(*S*)-A1.5** elutes at ~5.8 min.

2.4 Technoeconomic Analyses

Technoeconomic analyses were conducted to assess whether the observations in Section 2.3 could reduce **(*S*)-A1.5** (Fragment A) manufacturing costs. Costs of raw material inputs were calculated, process unit operations were mapped, along with their associated cycle times. This data was entered into the cost modeling tool developed and shared by Sia/LBG[5] to estimate total cost per kilogram including production costs at various conditions[6]. Replicate experiments at each temperature were averaged then used as the basis of comparison (percentage change), relative to the baseline (**Table 2.4.1**). The larger, 20g scale reaction was compared to the baseline separately from the smaller, 5g scale reactions. The combination of lowered reaction time and increased yield as a function of increased temperature resulted in the 80°C reactions having the lowest cost.[7]

[5] Latham Biopharm Group, part of Sia partners
[6] Modeling tools used to calculate total cost of processes using averages of manufacturing processes to estimate production costs in addition to raw material costs. Modelling tools have been used for COGs COE work recently.
[7] In experiments examining 100°C and 110°C initial incubation temperatures, reduced yields and new impurities (e.g., **A1.5-Amide**) were observed, negating the benefits of DKR cycle time reduction.

Table 2.4.1. Summary of estimated cost at each temperature tested.

Entry	ELN #	Initial Reaction Temperature	Scale	Total Time (hrs) [a]	Total Cost [b] ($/kg)	% Change [c]	Total Cost, Yield Held Constant [d]
1	SRK221-X2	60°C	5g	120	$1,287	n/a [baseline]	$994
2	BCH219-X3		5g	118	$1,389		$993
3	SRK221-X3	80°C	5g	66	$1,380	+12%	$967
4	SRK221-X5		5g	70	$1,614		$969
5	BCH219-X6		20g	114	$1,195	-11%	$991
6	BCH219-X1	100°C	5g	44	$1,714	+40%	$956
7	SRK221-X4		5g	42	$2,024		$955
8	BCH219-X2	100°C	5g	68	$1,655	+24%	$968

[a] Total time takes into account the setup through drying of the process assuming charging of raw materials at scale takes 0.5hrs. [b] Total cost calculated including manufacturing related using the Sia/LBG modeling tool to understand effects of varying temperature and reaction cycle time [c] Calculated based on the average of the two baseline experiments performed at 60°C. [d] Total cost calculated including manufacturing related using the Sia/LBG modeling tool varying total time and temperature while keeping yield at a constant 70%.

3 Conclusion

The purpose of this investigation was to ***1)*** articulate the scope and limitations of conducting the dynamic kinetic resolution of **A1.5** to **(*S*)-A1.5-NADL** at elevated temperatures, to ***2)*** estimate prospective operating cost savings viz-á-viz faster reaction rates, and to ***3)*** demonstrate an inline, manufacturing-suitable method for monitoring DKR progress. Studies summarized here enabled the following conclusions.

1) Regarding the scope and limitations of elevated-temperature DKR processes:
    - Reaction times decreased as a function of increasing preliminary incubation temperature. Reaction rate benefits, via higher initial incubation temperatures, were limited to 80°C. Experiments with an 80°C incubation temperature delivered the

best **(*S*)-A1.5** quality among the temperatures tested, beyond the 60°C baseline (wt% ~55% as the freebase, LCAP at 225 nm >95%, ee >98%).

- Beyond the 80°C optimum temperature – particularly, at or beyond 100°C:
  - New impurities formed in the DKR matrix (e.g., **A1.5-Amide**) and isolated product quality was diminished (informed by wt% assay data).
  - Enantiomeric excess decreased, markedly (ee <98%).

2) Regarding prospective operating cost savings enabled by faster reaction rates
   - This work affirmed that shorter reaction times are achievable by enacting higher temperature incubation periods at DKR onset. This has the potential to positively impact overall cycle time and reduce OpEx (Operating Expense) in a manufacturing facility. At the optimal observed temperature (80°C), small-scale (5g) reactions were estimated to have a higher cost than the baseline (yield effects) while the 20g experiment had an 11% estimated cost reduction (with extended duration to achieve $\Delta A1.5_{6h} = 0$). Please see the bullet point below for further discussion on this topic.
   - To further optimize for DKR brevity and higher yield – i.e., to bridge disparate productivity between 5g and 20g experiments at 80°C – further examination and control of mixing and mass transfer phenomena is required (e.g., via impeller selection, stir rates, baffle integration and positioning, reactor V_{min} and V_{max}, etc.).
3) Regarding demonstration of an inline analytical method for following DKR progression
   - PAT (ReactIR) provided an effective way to monitor the reaction progress of the conversion of racemic **A1.5** to enantiopure **(*S*)-A1.5-NADL**. Unexpected phenomena in PAT implementation were documented, analyzed, and resolved, facilitating the use of this approach in industrial practice.
     - Disparities between ReactIR- and GC-MS-determined **A1.5** concentrations were attributed to agglomeration of a film on the probe window. Periodic rinsing of the probe was an effective remedy. Further assessment and optimization of mixing and mass transfer, as mentioned above, is anticipated to bring benefits here, as well.

4 Methods

4.1 Analytical Methods

4.1.1 ReactIR

A Mettler Toledo ReactIR with a DiComp, 9.5mm x 305mm x 1.5m probe was used to create a 6-point IR calibration. **A1.5** standards between 5 mg/mL and 50 mg/mL prepared in toluene and measured at ambient temperature were used for the calibration. A toluene blank was used for the 0 mg/mL calibration point. Peak height and peak area were both monitored. The full IR spectra for the toluene and **A1.5** standard can be found in **Figure 4.1.1.1**.

As discussed in Section 2.2, once the IR probe became covered in the gelatinous film the readouts lead to an incorrect assumption of reaction completion. This is true regardless of the univariate or multivariate calibration techniques. For future experiments the steps below can be taken to minimize this issue:

- Expand the spectral region to enable partial least squares (PLS) to model other reaction components. This may be the full spectral range or a combination of several smaller regions.
- Investigate other preprocessing methods which could include normalization to a toluene peak to correct for IR probe fouling.
- Include reaction data in the training and test sets.
- Check the efficiency of the proposed modeling approaches with more in-depth data analysis approaches.

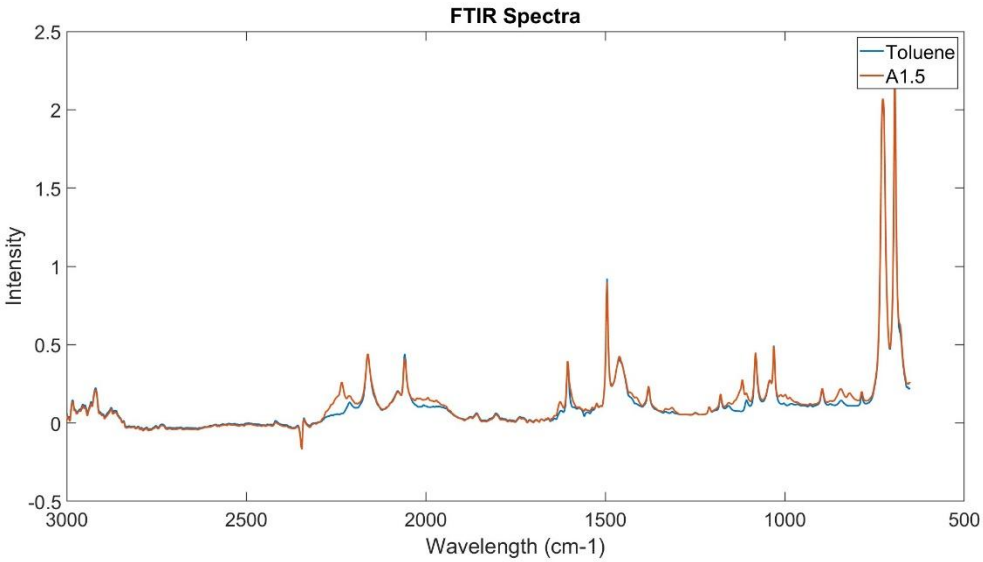

Figure 4.1.1.1. IR spectra of **A1.5** standard and toluene collected at ambient temperature.

4.1.1.1 ReactIR Univariate Calibration

The reaction was monitored by IR (Mettler-Toledo ReactIR 702L) using a selective peak at 820 cm^{-1} which is unique to the soluble form of **A1.5** in toluene as **A1.5** or the **(R)-A1.5-NADL** (**Figure 4.1.1.1.1**). IR calibration using both peak area and peak height were linear, $R^2 > 0.99$ (**Figure 4.1.1.1.2**). Profiling the selected peak height or peak area value versus time shows the estimated concentration of the soluble form of **A1.5** in toluene in real-time.

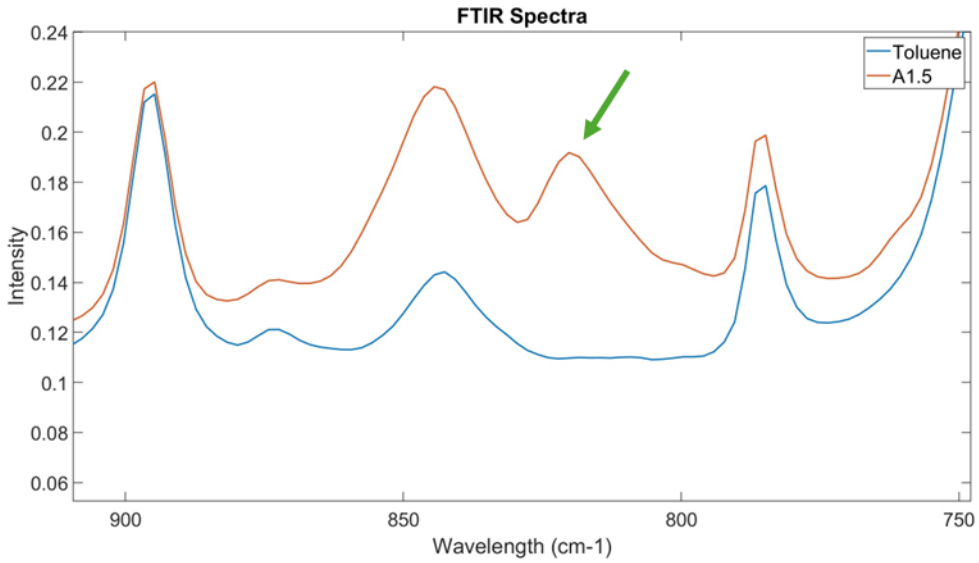

Figure 4.1.1.1.1. IR spectra of standard **A1.5** and toluene depicting the peak unique to **A1.5** at 820 cm^{-1} (green arrow points to this peak).

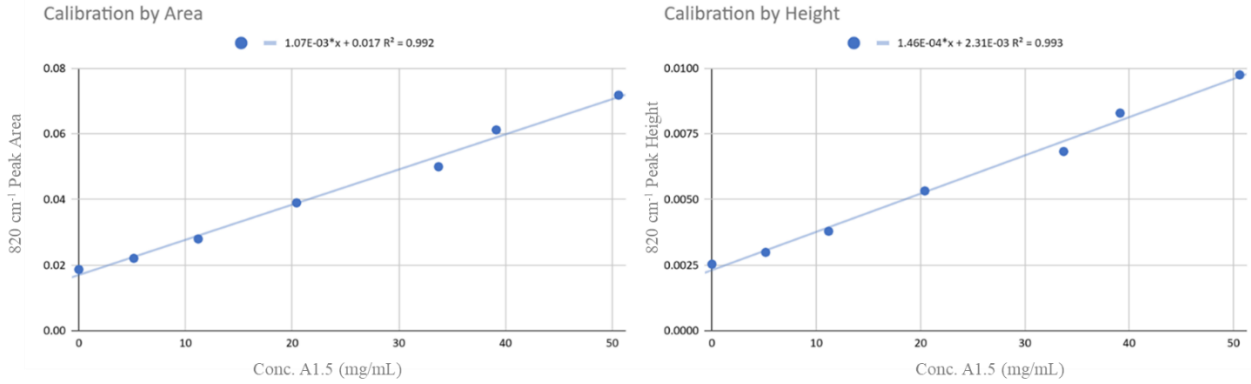

Figure 4.1.1.1.2. IR calibration curves by peak area (left) or peak height (right) were both linear (R^2 >0.99).

4.1.1.2 ReactIR Multivariate Calibration (Partial Least Squares Model)

PLS modeling was performed off-line after reaction completion (MatLab with PLS Toolbox application). The calibration data set was used for model training and test testing. Two thirds of the calibration data was dedicated to the training set and the remaining one third to the test set. The Automatic Whittaker Filter (AWF) preprocessing method was applied to the IR data to

improve modeling statistics. Modeling was performed using the IR spectrum from the selected region of 825 to 815 cm^{-1} as a model. Using the entire range from 3000 to 650 cm^{-1} lead to a higher deviation in predicted concentrations at the low end which was the area of interest (**Figure 4.1.1.2.1**), i.e. the model exhibited overfitting at lower concentrations (**Figures 4.1.1.2.2 through 4.1.1.2.6**). The reduced wavelength range model was much less dispersing at lower concentrations (**Figure 4.1.1.2.1)**.

Statistical criteria values are representative of modeling success, the root mean square error calibration (RMSEC=1.72), root mean square error cross-validation (RMSECV=1.94), root mean square error prediction (RMSEP=1.58), calibration bias (-0.018) , cross-validation bias (-0.004), prediction bias (0.005), correlation coefficient calibration (R^2 Cal=0.99), correlation coefficient cross-validation (R^2 CV=0.99), and correlation coefficient prediction (R^2 Pred=0.99) (**Figure 4.1.1.2.1)**. The predicted concentration profiles by PLS matched and were consistent with the concentration profiles obtained from the peak height or peak area.

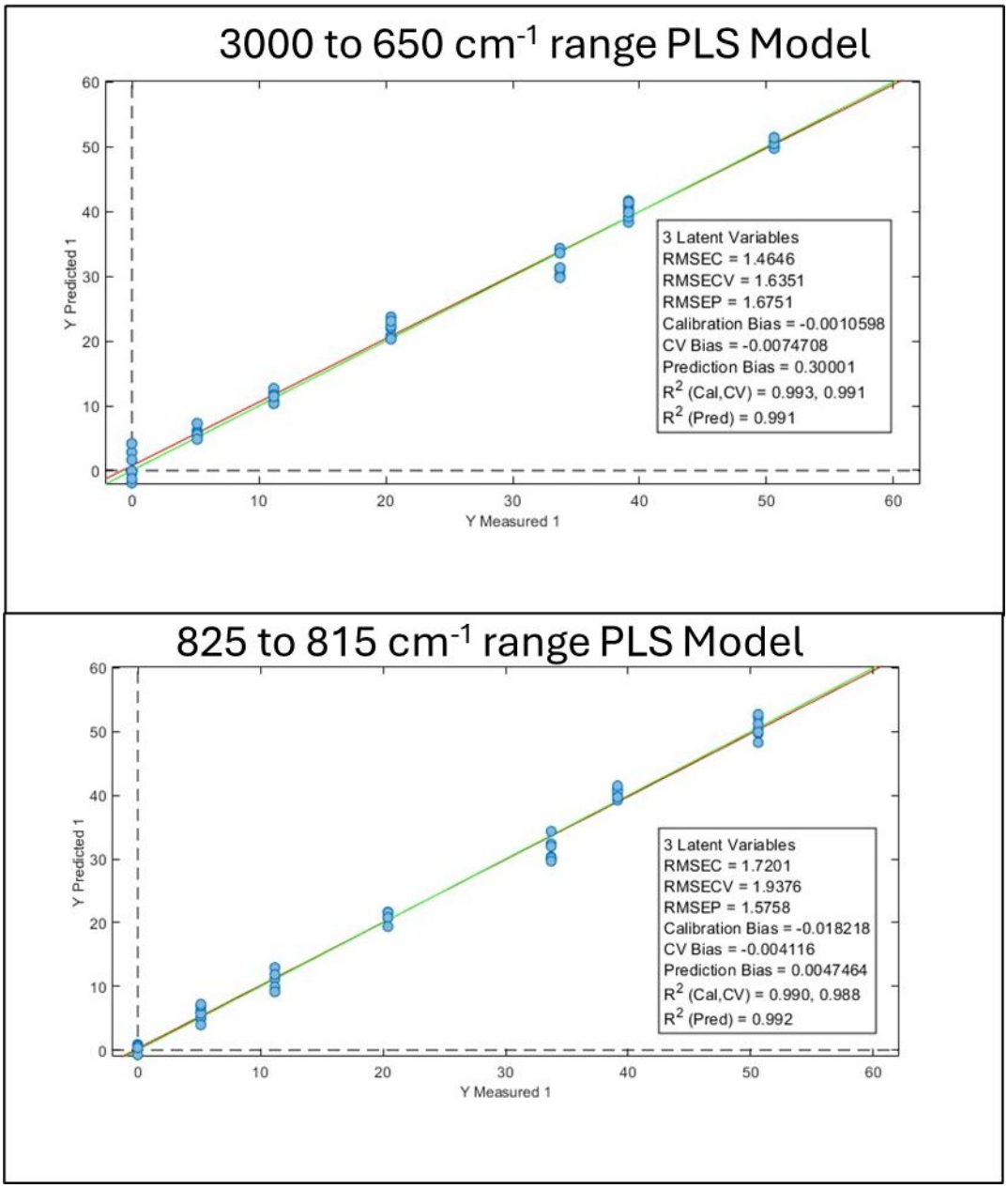

Figure 4.1.1.2.1. Predicted vs. measured concentration of **A1.5** by PLS depicting the validity of the model for full IR spectrum (top) and reduced range (bottom).

Figure 4.1.1.2.2. Overlay of predicted concentration by full IR range PLS model (blue) and selected range PLS model (orange). All data is plotted against time (hours) to show correlation between modelled data and gathered experimental data. Plot for 60°C conditions (5g).

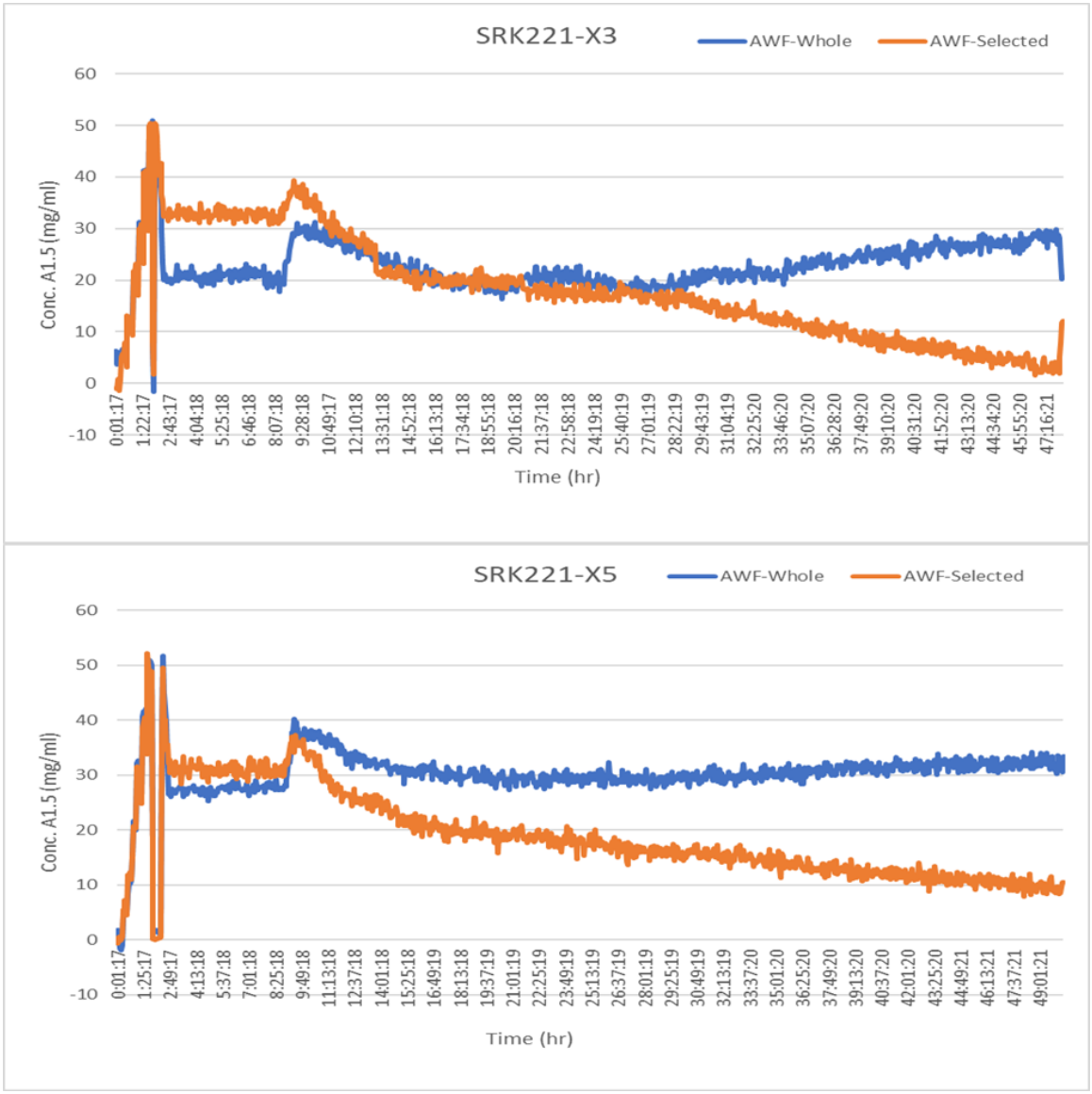

Figure 4.1.1.2.3. Overlay of predicted concentration by full IR range PLS model (blue) and selected range PLS model (orange). All data is plotted against time (hours) to show correlation between modelled data and gathered experimental data. Plot for 80ºC conditions (5g).

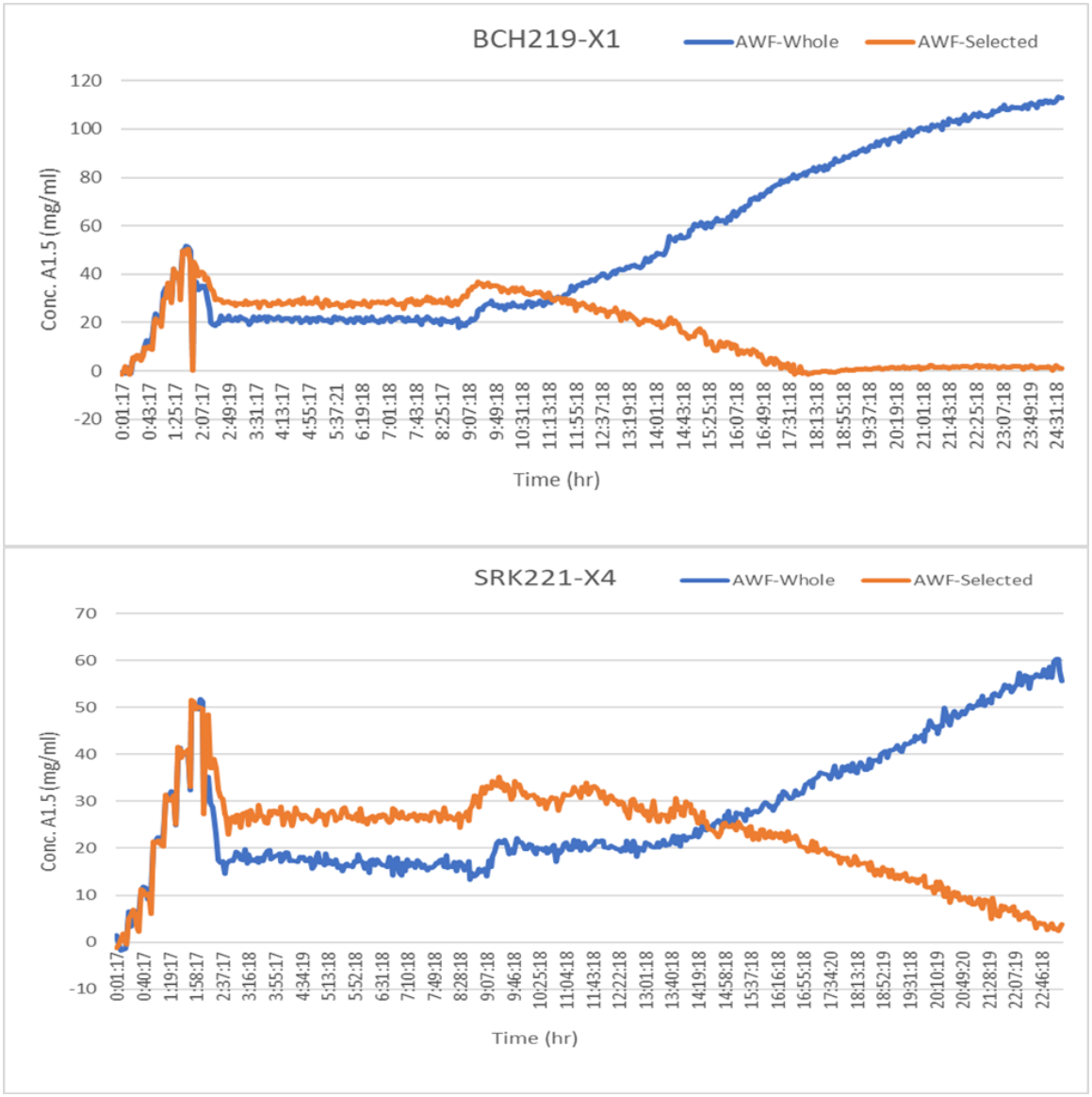

Figure 4.1.1.2.4. Overlay of predicted concentration by full IR range PLS model (blue) and selected range PLS model (orange). All data is plotted against time (hours) to show correlation between modelled data and gathered experimental data. Plot for 100ºC conditions (5g).

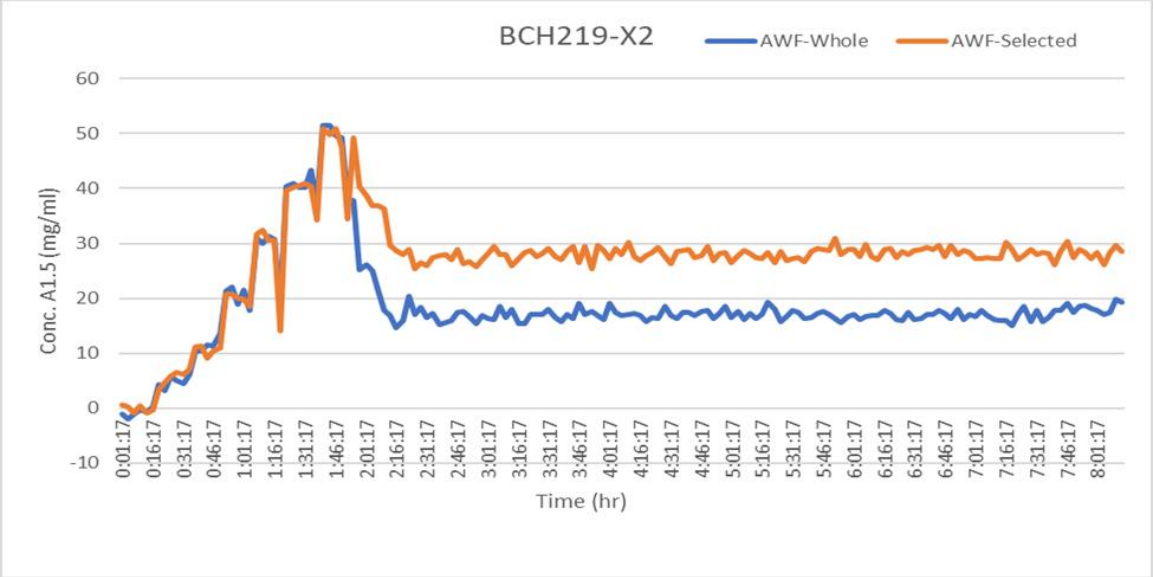

Figure 4.1.1.2.5. Overlay of predicted concentration by full IR range PLS model (blue) and selected range PLS model (orange). All data is plotted against time (hours) to show correlation between modelled data and gathered experimental data. Plot for 110ºC conditions (5g).

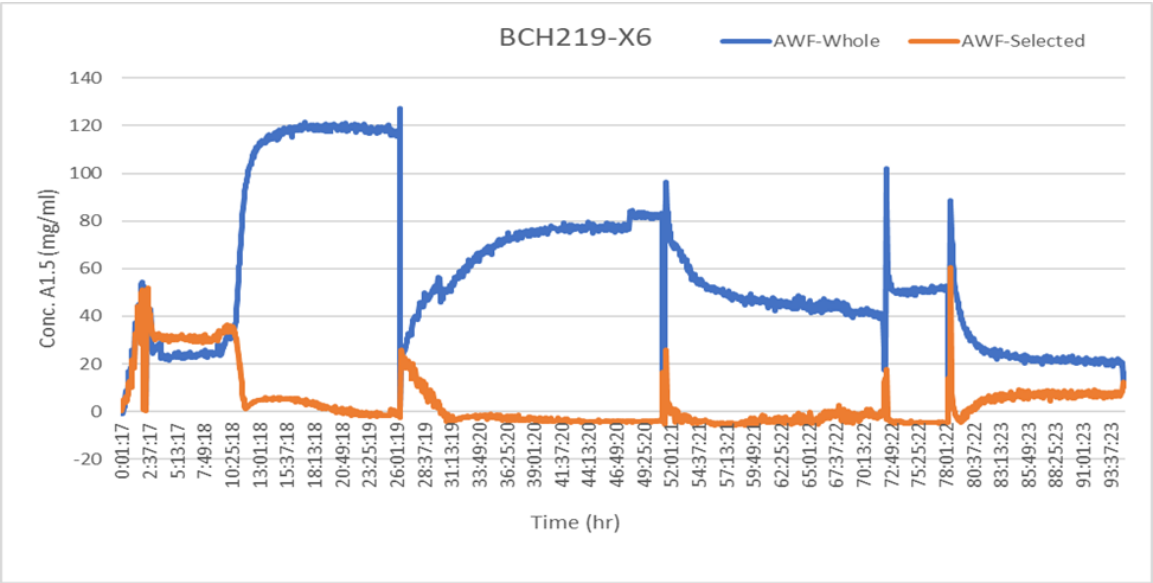

Figure 4.1.1.2.6. Overlay of predicted concentration by full IR range PLS model (blue) and selected range PLS model (orange). All data is plotted against time (hours) to show correlation between modelled data and gathered experimental data. Plot for 80ºC conditions (20g).

4.1.2 GC-MS

The GC-MS (Agilent 8890 gas chromatograph (GC) with a 5977 mass spectrometer detector (MSD)) method utilized a J&W HP-5ms GC Column (30m x 0.25mm x 0.25mm) with a helium flow rate of 0.92 mL/min and a split ratio of 100:1. The initial temperature was set to 50ºC for 3 minutes followed by a 25ºC/min ramp to 250ºC and held for 3 minutes. The final ramp to 300ºC was done at 25ºC/min and held for 3 mins for a total runtime of 19 min. A 1 mL injection was used. GC-MS was used over LC-UV for in-process confirmation due to the presence of toluene in the samples (**Figure 4.1.2.1)**. In depth method details can be found in Len Frag A PDR (August 2024).[18]

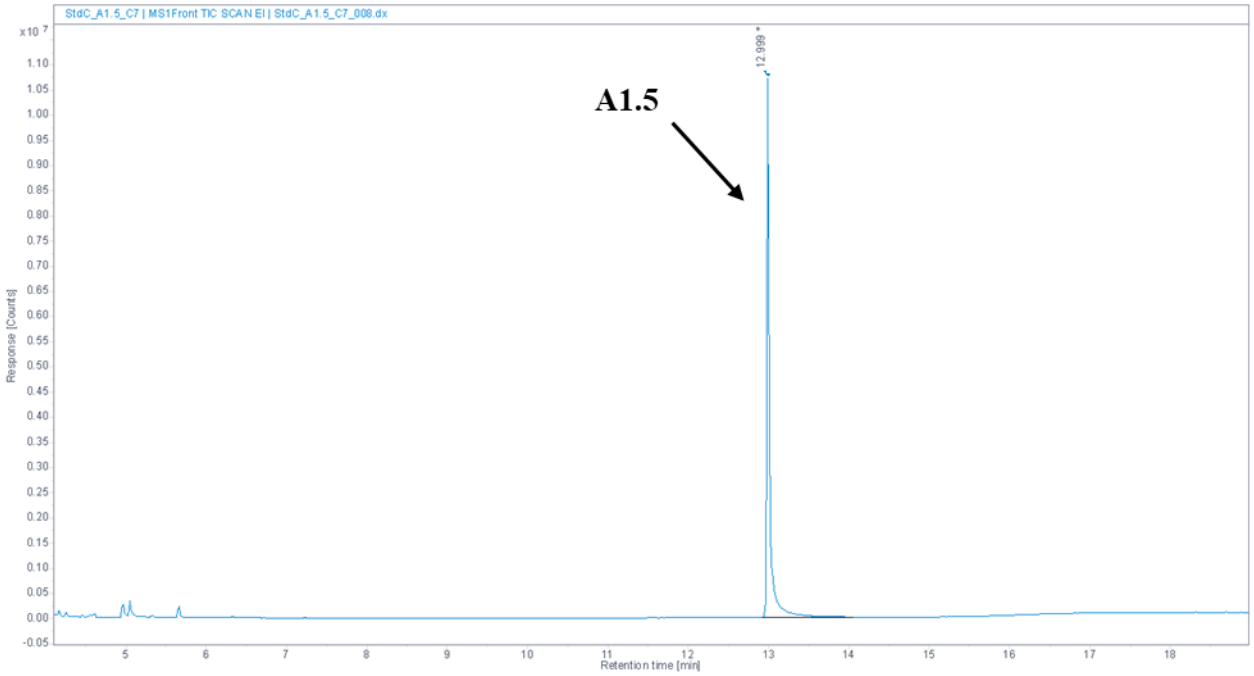

Figure 4.1.2.1. Representative GC-MS chromatogram of an **A1.5** standard (1 mg/mL), retention time of ~13 minutes. GC-MS was used as a secondary method to the IR data for concentration determination.

4.1.3 LC-UV

For final weight assay, LC-UV (Agilent 1200 LC) was used. A binary mobile phase gradient was used for elution with mobile phase A consisting of 25 mM potassium phosphate, pH 8 and mobile phase B consisting of methanol. Initial conditions were set to 40% B and held constant for 0.5 minutes and then ramped to 90% over 9.5 minutes. This was held for 15 minutes. Diode array detection was used with a detection wavelength of 225 nm (**Figure 4.1.3.1**). In depth method details can be found in Len Frag A PDR (August 2024).[18]

For solid analysis, solutions were made at a concentration of approximately 1 mg/mL in acetonitrile. For each solid sample, duplicate preparations were made and each preparation was injected twice. Calibration was done using an external standard with a 7-point calibration curve. Calibration curves were assessed for linearity to determine if any points were to be excluded. Both **NADL** and **A1.5** were assayed.

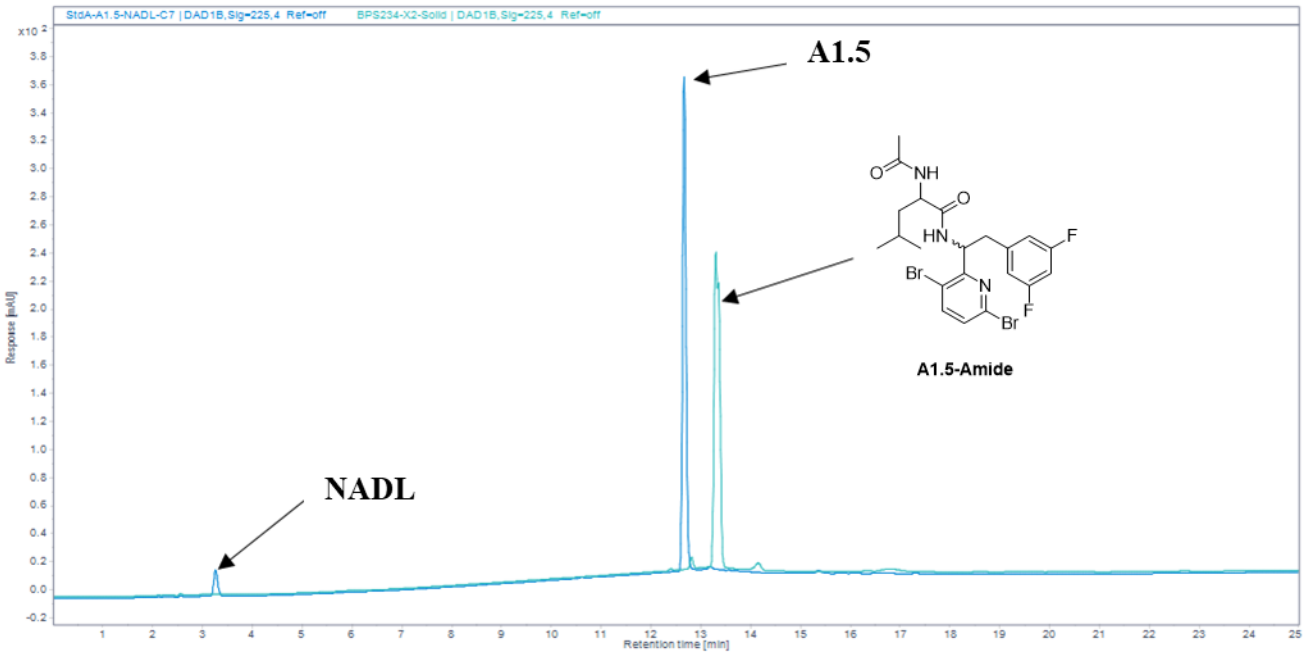

Figure 4.1.3.1. Representative LC-UV spectrum of using standards of **A1.5** (1 mg/mL)**, NADL** (1mg/mL) and **A1.5-Amide** impurity (1 mg/mL). **A1.5** elutes at 12.8 mins, **NADL** elutes at 3.2 mins and **A1.5-Amide** impurity elutes at 13.2 min.

4.1.4 SFC-UV

SFC analysis with UV detection (Agilent 1260 SFC) was performed to measure enantiomeric purity (**Figure 4.1.4.1**). In depth method details can be found in Len Frag A PDR (August 2024).[18]

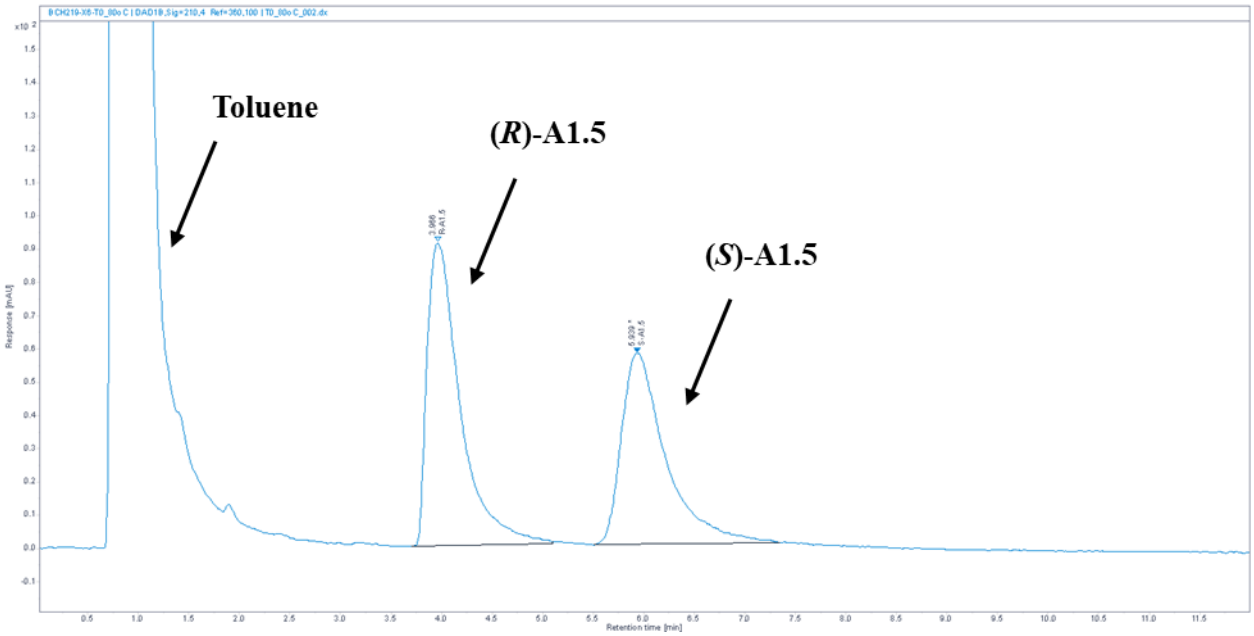

Figure 4.1.4.1. Example SFC-UV chromatogram of the reaction mixture at T=0. Isomers are in a roughly 1:1 ratio. **(R)-A1.5** is ~4 min and **(S)-A1.5** is ~6 min. The unintegrated peak is toluene. Sample concentration was 5 mg/mL.

4.1.5 TGA

Residual solvent was determined using TGA (Texas Instruments Discovery SDT 650). Acquisition parameters were set as follows: the sample was equilibrated at 25°C for 1 minute followed by a ramp of 10°C/min to 120°C followed by a hold at 120°C for 10 minutes. No trend was observed based on the initial DKR set temperature as the final mass loss should only be a factor of drying conditions (**Table 2.3.5.1**).

Table 4.1.5.1. Summary mass loss by DSC/TGA mass loss data

Entry	ELN #	Scale	Initial Reaction Temperature (°C)	Mass Loss (%)
1	SRK221-X2	5g	60°C	0.25%
2	BCH219-X3	5g		0.14%
3	SRK221-X3	5g	80°C	0.41%
4	SRK221-X5	5g		0.09%
5	BCH219-X6	20g		0.26%
6	BCH219-X1	5g	100°C	0.33%
7	SRK221-X4	5g		0.12%
8	BCH219-X2	5g	110°C	0.42%

4.1.6 LC-MS

Similar conditions were used for LC-MS (Agilent 1260 LC and 6125 mass spectrometer) analysis. However, the potassium phosphate buffer was replaced with an ammonium carbonate buffer to be MSD compatible (**Figures 4.1.6.1** and **4.1.6.2**). In depth method details can be found in Len Frag A PDR (August 2024).[18]

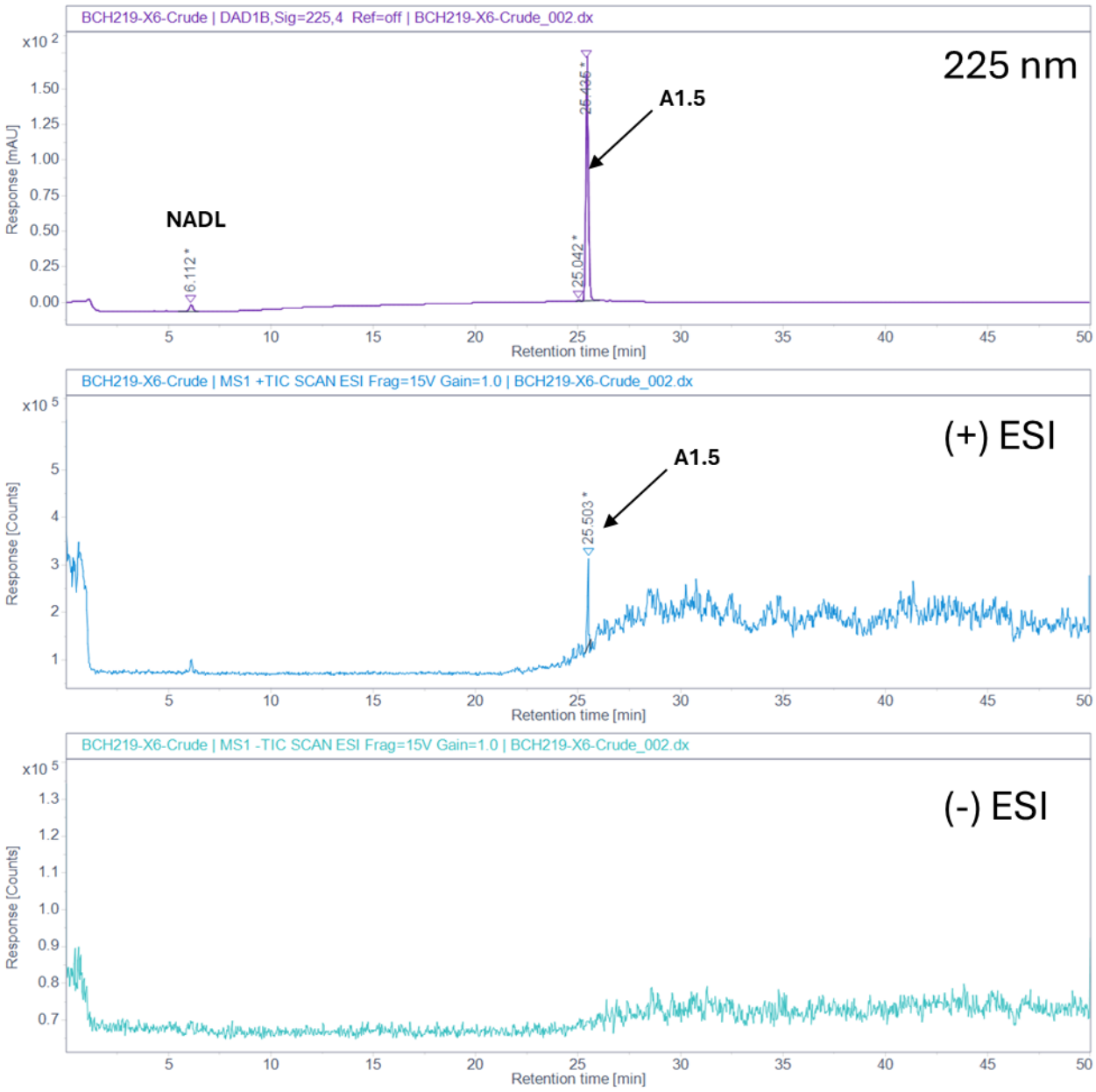

Figure 4.1.6.1. Example LC-MS chromatogram for **A1.5**. LC-MS was used to confirm the mass of any new impurities observed (80ºC reaction temperature, 20g scale.). Sample concentration was 1 mg/mL.

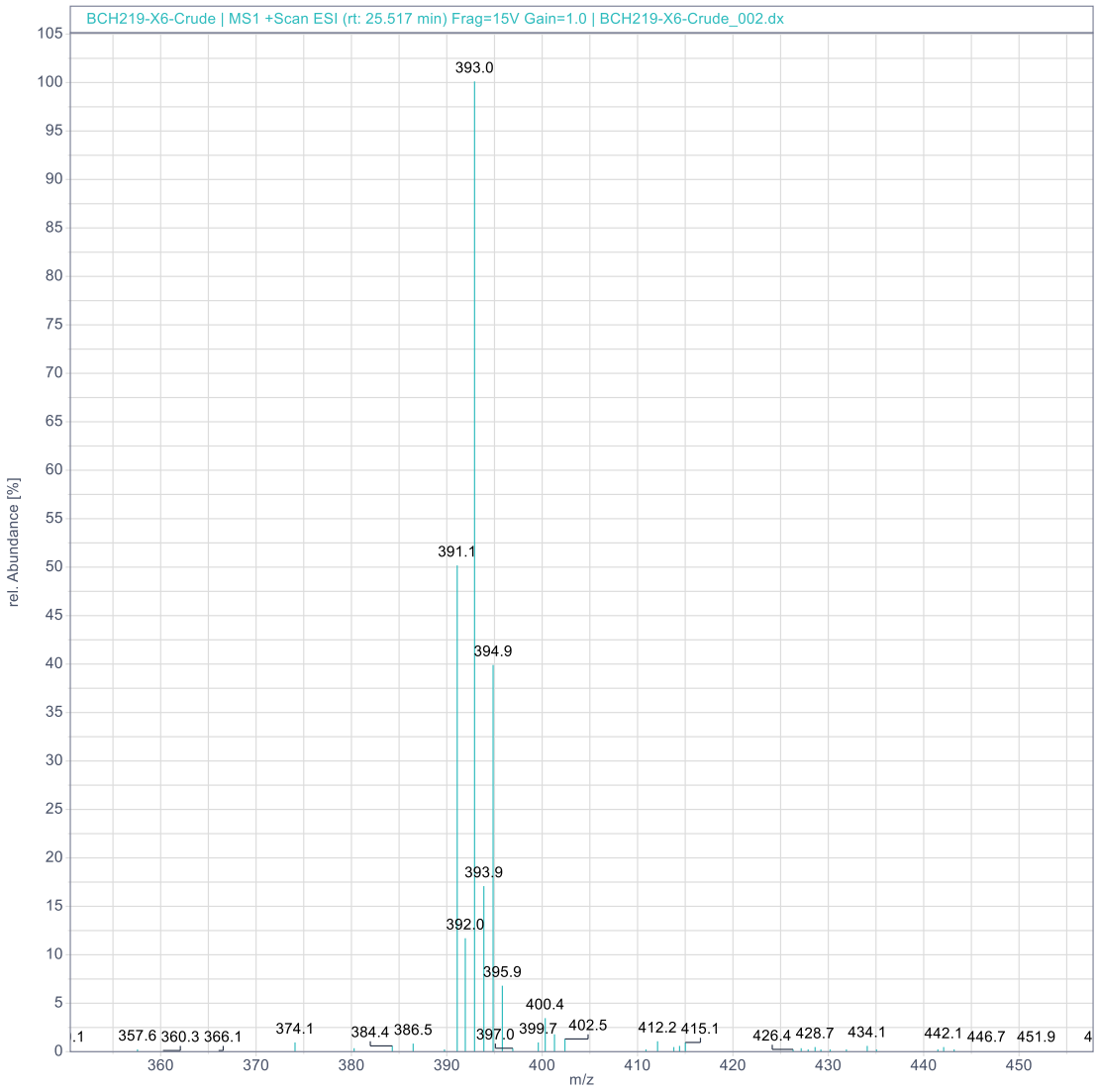

Figure 4.1.6.2. Positive mass spectrum of **A1.5** showing (2) bromine isotope pattern.

4.2 Synthetic Procedures

4.2.1 General

Reagents and solvents were obtained from commercial suppliers and used as received unless otherwise indicated. Where applicable, reactions were conducted in oven-dried (120 °C) glassware, which was assembled while hot, and cooled to ambient temperature under an inert atmosphere. Reactors were pre-rinsed with reaction solvent and subjected to evacuation/back-fill cycles (3×) as necessary. Reactions were monitored by TLC (precoated silica gel 60 F254 plates,

EMD Chemicals), ReactIR, Agilent GCMS or crude ^{1}H NMR. HRMS was recorded using Perkin Elmer Axion 2 ToF MS, ionization mode: positive with scan range: 100 - 1000 m/z, flight tube voltage: 8 kV, spray voltage: 3.5 kV, solvent: methanol. TLC was visualized with UV light. Proton (^{1}H NMR), carbon (^{13}C NMR) and 2-DNMR spectra of the compounds were recorded on Bruker Avance III HD Ascend 600 MHz spectrometer. NMR solvents used were DMSO-d_6, $CDCl_3$ and CD_3OD. Chemical shifts were reported in parts per million (ppm). Coupling constants J were reported in hertz (Hz). The abbreviations used to designate signal multiplicity were: s, singlet; d, doublet; t, triplet; q, quartet, p, pentet; dd, doublet of doublets; ddd, doublet of doublet of doublets; dt, double of triplets; ddt, doublet of doublet of triplets; m, multiplet; br, broad.

4.2.2 Typical DKR procedure, example with a 20-gram scale reaction (entry 5 (BCH219-X6) in **Table 2.1.1**)

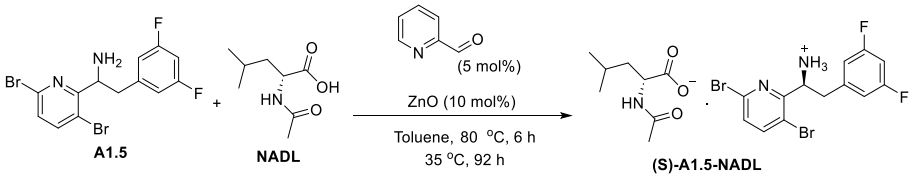

In a clean 1000 ml 4-necked round-bottom flask, 1-(3,6-dibromopyridin-2-yl)-2-(3,5-difluorophenyl)ethan-1-amine (20.0 g, 97% wt, 1.0 eq, 49.5 mmol) was added along with toluene (400 ml; 20 V). The resulting mass was stirred with an overhead stirrer, keeping the temperature below 25°C until it became homogeneous. (*R*)-Ac-2-amino-4-methylpentanoic acid (11.0 g, 97% wt, 1.2 eq, 61.86 mmol) and zinc oxide (410.9 mg, 77.4 µL, 98% wt, 0.1 eq, 4.9 mmol) were added in succession to the above mass in single portions. To the resulting solution pyridine-2-carboxaldehyde (265.3 mg, 235.6 µL, 99.9% wt, 0.05 eq, 2.5 mmol) was added as a solution in toluene (100 ml; 5.0 vol.). The reaction mass was warmed to 80-85°C and maintained for 6 hours by monitoring through IR-Probe. After 6 hours maintaining the stated internal temperature, the reaction mass was cooled to 35-37°C and the reaction progress was further monitored by React-IR. After 86 hours (total 92 hours, including the maintenance period at 80°C), the reaction was stopped and cooled to 20-25°C. The reaction mass was filtered and the solid remaining in the RB-flask was transferred by slurrying with toluene (200 ml, 10 V). The wet cake was slurry washed

with toluene (2×70 ml, 7 V). Resulting wet cake was aspirated for 5 minutes to partially dry then transferred into a clean, dry 1000 mL RBF to which toluene was added (400 ml; 20 V). The resulting heterogeneous mass was stirred at 25°C for 90 minutes. The solution was filtered and the wet cake was washed with toluene (2×130 ml, 13 V). The wet solid was dried under vacuum at less than 60 °C to a constant weight (19.63 g, 56.1 % wt, 58% isolated yield).

4.2.3 Synthesis of the **A1.5-Amide** impurity

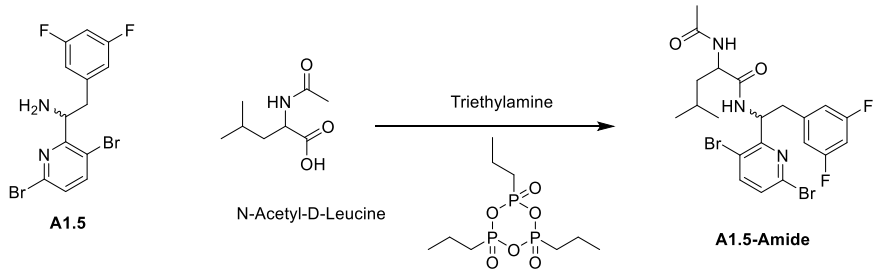

A solution of A1.5 (1.48 g, 3.72 mmol, 1 eq), N-acetyl-D-leucine (NADL, 1.03 g, 3.85 mmol, 1.03 eq), and triethylamine (1.5 mL, 10.8 mmol, 2.9 eq) in acetonitrile (15 mL) was stirred at 0°C. n-propanephosphonic acid anhydride (T3P, 50% solution in acetonitrile, 3.3 g, 5.67 mmol, 1.5 eq) was added dropwise. The reaction mixture was allowed to warm to room temperature and was stirred for 16 h. The reaction mixture was quenched with water (20 mL). The precipitated product was filtered and the filter cake was dried to afford **A1.5-Amide** as a white solid (1.73 g, 84.8% isolated yield).

^{1}H NMR (600 MHz, $CDCl_3$) δ 7.67 (t, J = 8.6 Hz, 1H), 7.28 (dd, J = 8.3, 4.4 Hz, 1H), 7.08 – 6.95 (m, 1H), 6.71 – 6.57 (m, 3H), 5.78 (t, J = 8.3 Hz, 1H), 5.69 (dtd, J = 33.9, 8.2, 5.8 Hz, 1H), 4.55 – 4.37 (m, 1H), 3.12 (dt, J = 12.5, 6.1 Hz, 1H), 3.01 – 2.89 (m, 1H), 2.01 (d, J = 14.9 Hz, 3H), 1.64 – 1.48 (m, 2H), 1.46 – 1.36 (m, 1H), 0.94 – 0.85 (m, 6H).

MS (+ ESI) *m/z*: $[M+H]^+$ calcd for $C_{21}H_{23}Br_2F_2N_3O_2 \cdot H^+$, 546.0; found: 546.1.

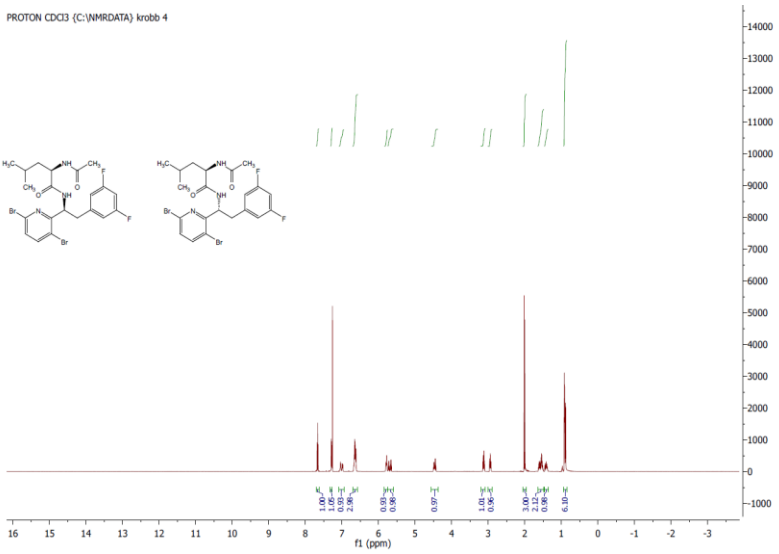

Figure 4.2.3.1. Proton NMR spectrum of **A1.5-Amide** impurity.

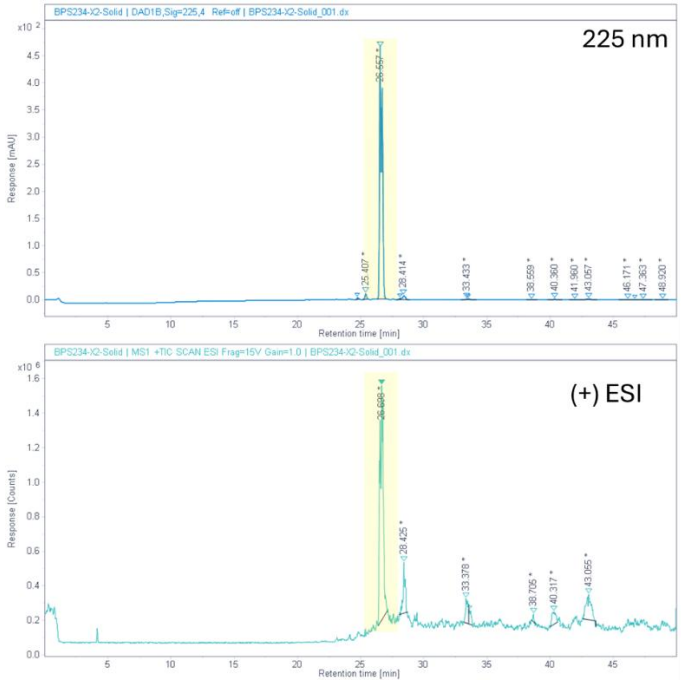

Figure 4.2.3.2. LC-MS chromatogram of **A1.5-Amide** impurity. Peak splitting is observed due to the presence of both isomers.

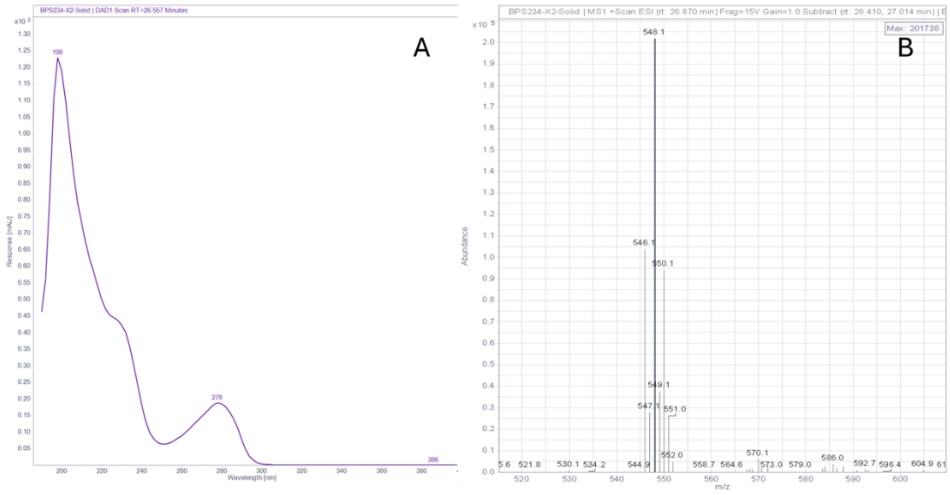

Figure 4.2.3.3. A) UV spectrum of **A1.5-Amide** impurity at retention time 26.6 min. B) Positive mass spectrum of **A1.5-Amide** impurity showing (2) bromine isotope pattern at retention time 26.6 min.

5 Appendix

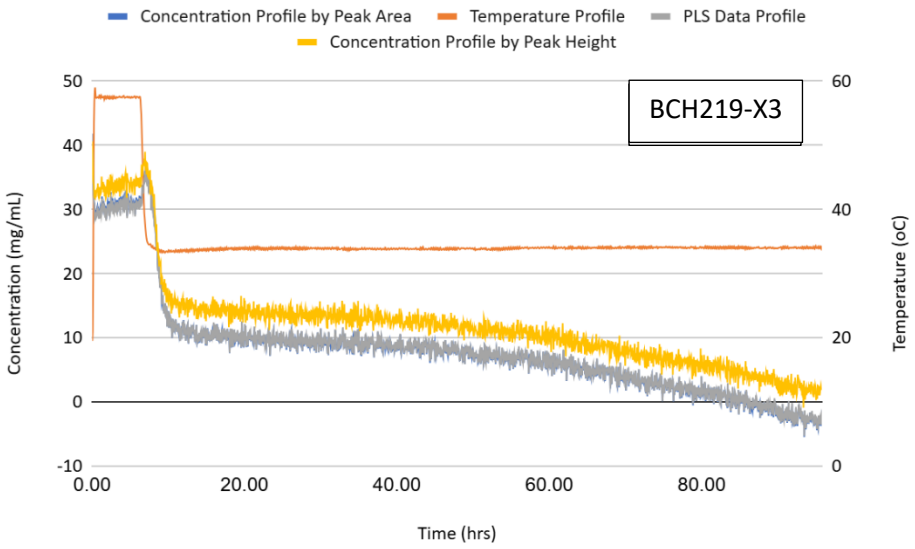

Figure 5.1. Overlay of temperature profile (orange), concentration by peak area (blue), concentration by peak height (grey), and PLS modeling data (yellow) for BCH219-X3. All data is plotted against time (hours) to show correlation between modeled data and gathered experimental data. Plot for 60°C conditions.

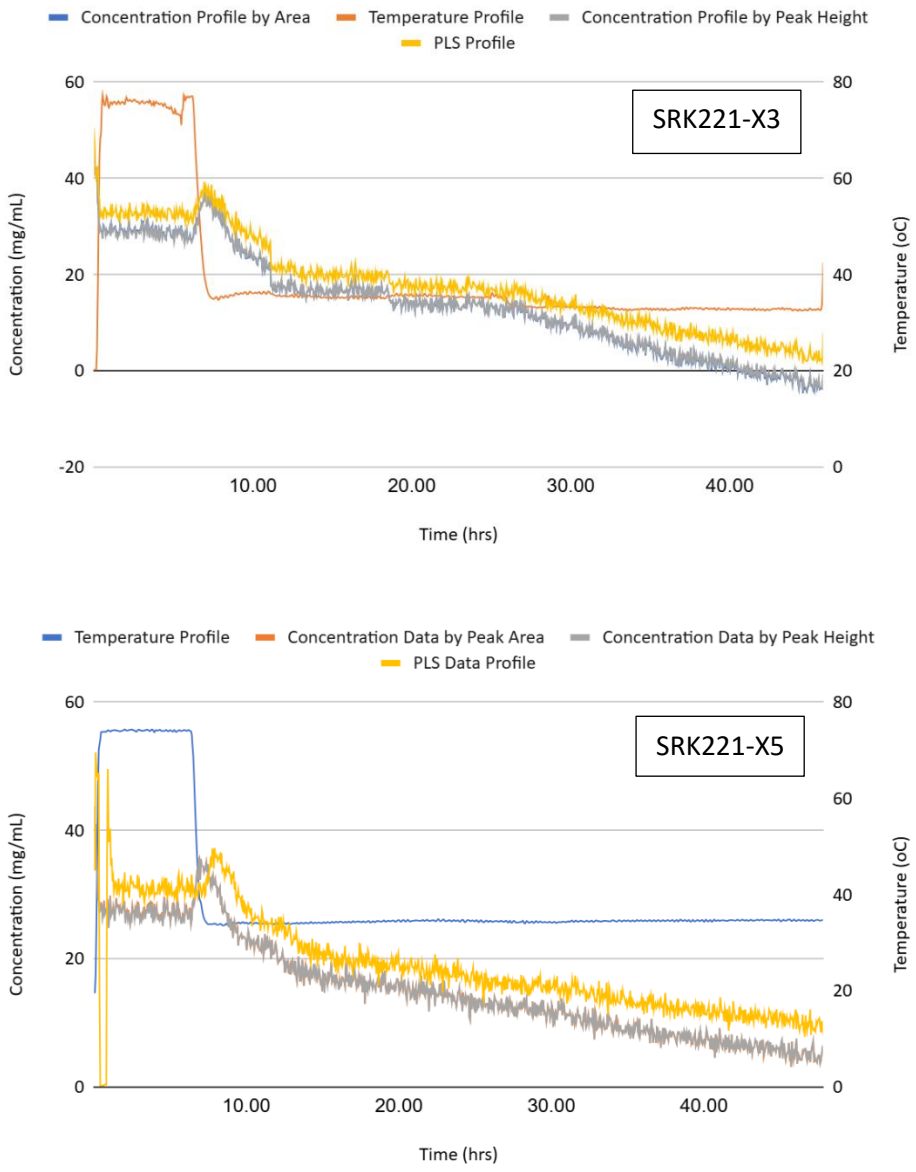

Figure 5.2. Overlay of temperature profile (orange), concentration by peak area (blue), concentration by peak height (grey), and PLS modeling data (yellow) For SRK221-X3 and SRK221-X5. All data is plotted against time (hours) to show correlation between modeled data and gathered experimental data. Plot for 80ºC conditions.

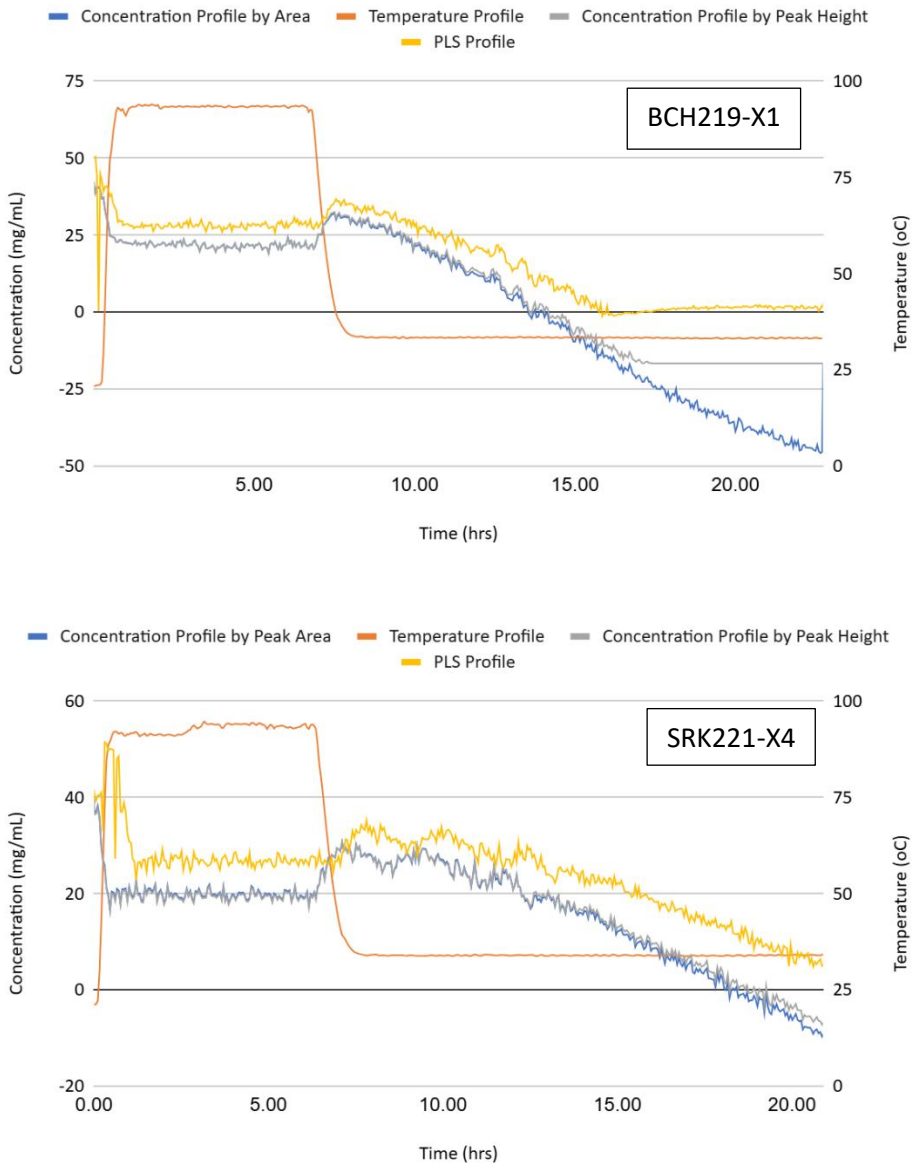

Figure 5.3. Overlay of temperature profile (orange), concentration by peak area (blue), concentration by peak height (grey), and PLS modeling data (yellow) for BCH219-X1 and SRK221-X4. All data is plotted against time (hours) to show correlation between modeled data and gathered experimental data. Plot for 100°C conditions.

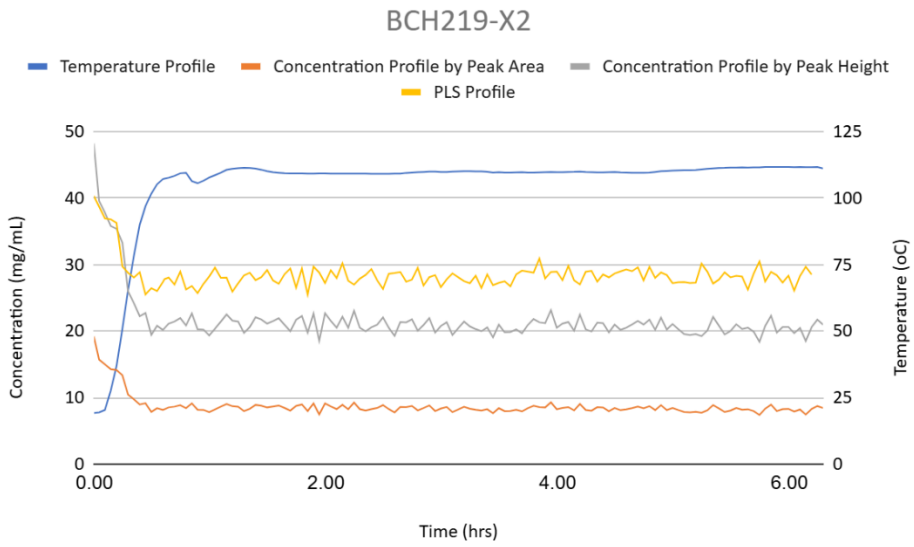

Figure 5.4. Overlay of temperature profile (orange), concentration by peak area (blue), concentration by peak height (grey), and PLS modeling data (yellow) for BCH219-X2. All data is plotted against time (hours) to show correlation between modeled data and gathered experimental data. Plot for 110°C conditions.

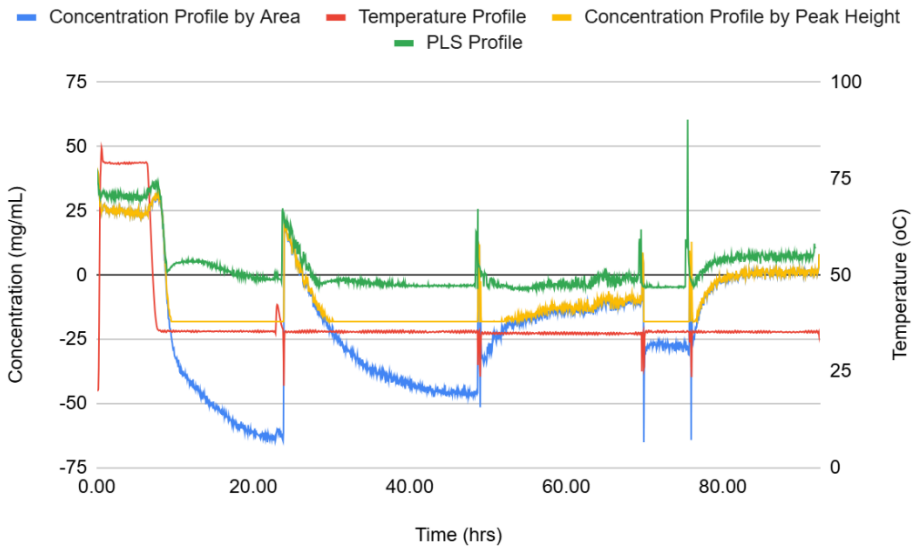

Figure 5.5. Overlay of temperature profile (red), concentration by peak area (blue), concentration by peak height (yellow), and PLS modeling data (green) for BCH219-X6. All data

is plotted against time (hours) to show correlation between modeled data and gathered experimental data. Plot for 80°C condition at the 20g reaction scale. The effect of the film on the IR probe seen by the rapid changes in the concentration.

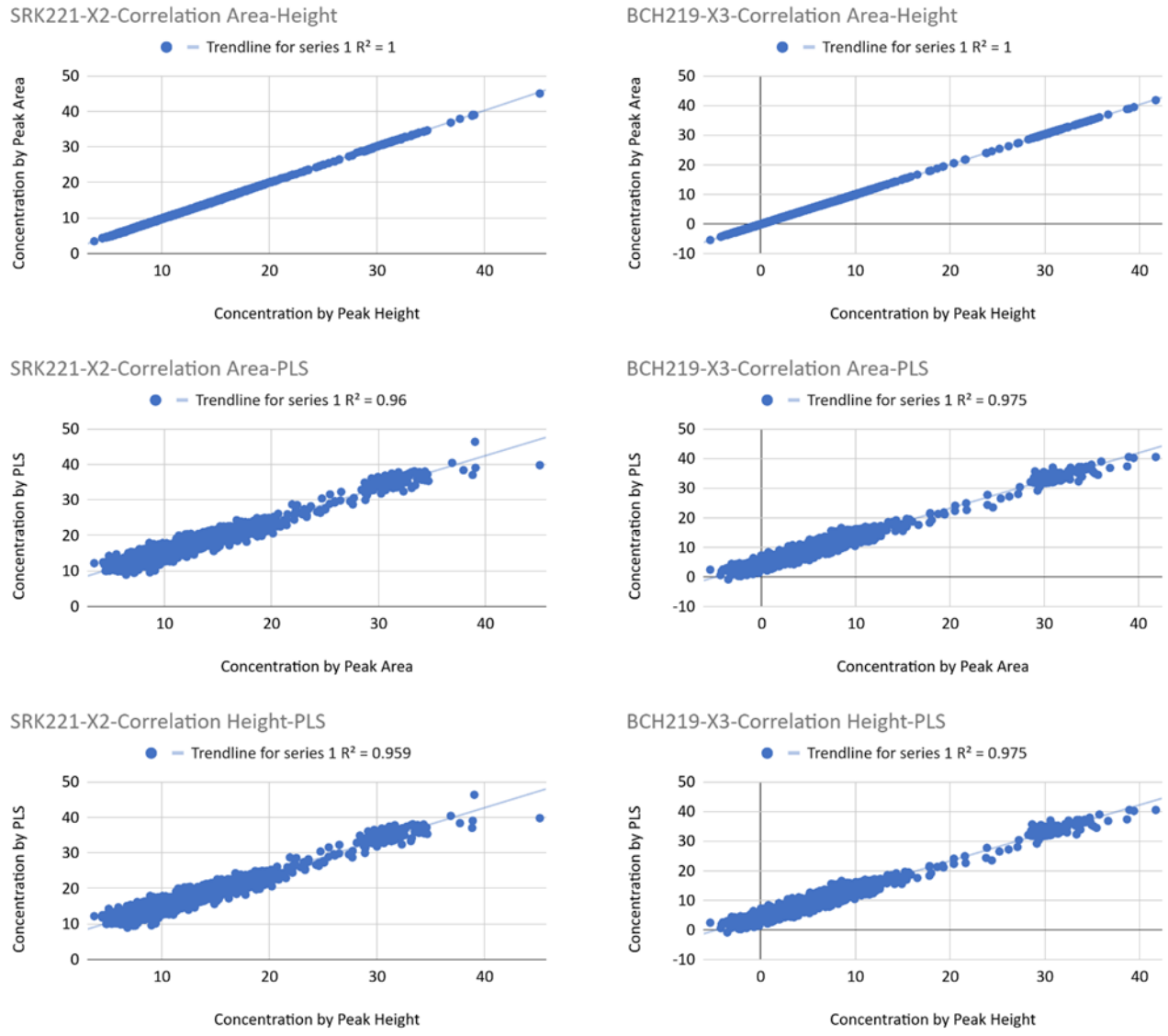

Figure 5.6. R^2 similarity correlation between peak area, peak height and the reduced range PLS model for 60°C, 5g.

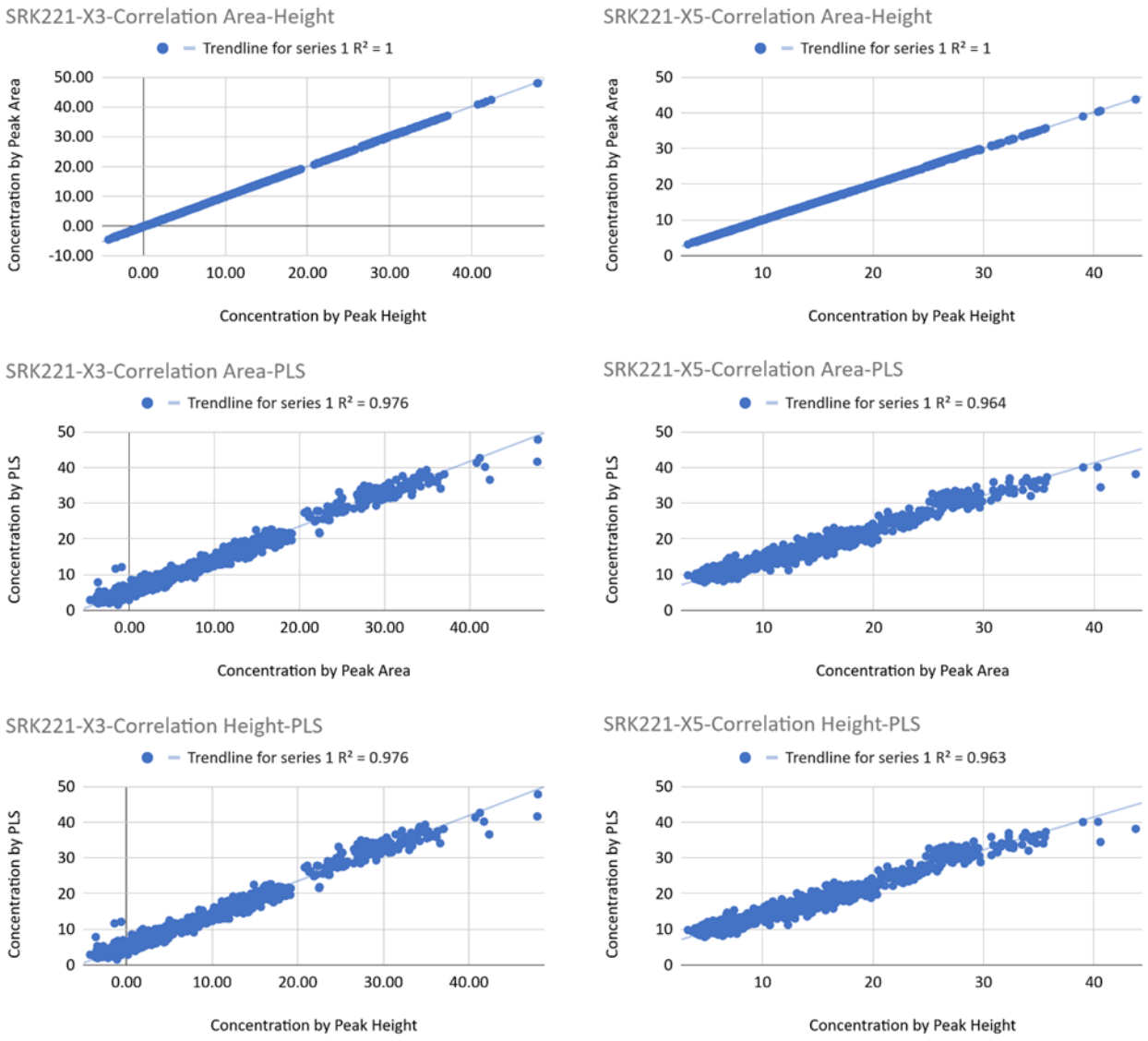

Figure 5.7. R^2 similarity correlation between peak area, peak height and the reduced range PLS model for 80°C, 5g.

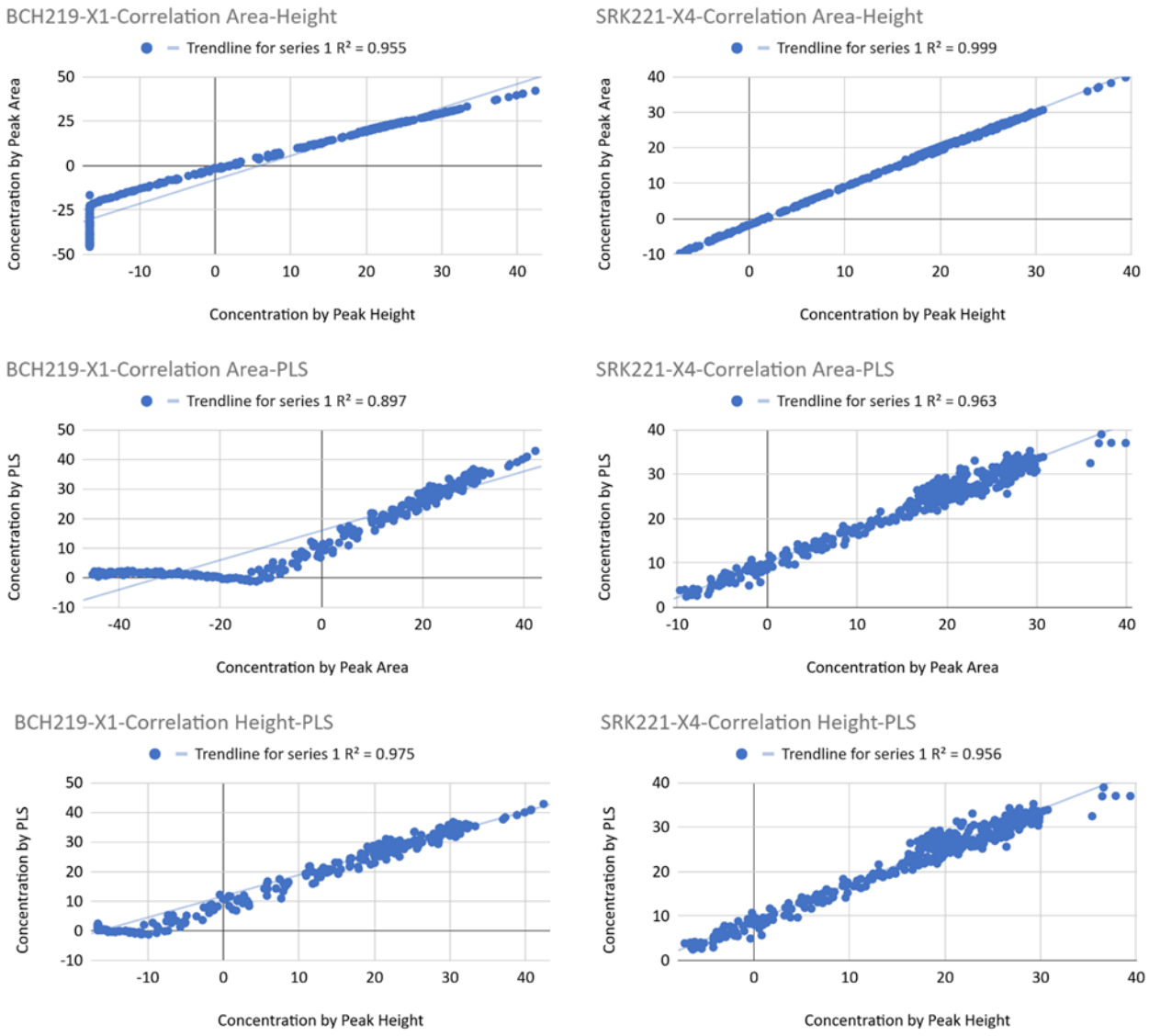

Figure 5.8. R^2 similarity correlation between peak area, peak height and the reduced range PLS model for 100°C, 5g.

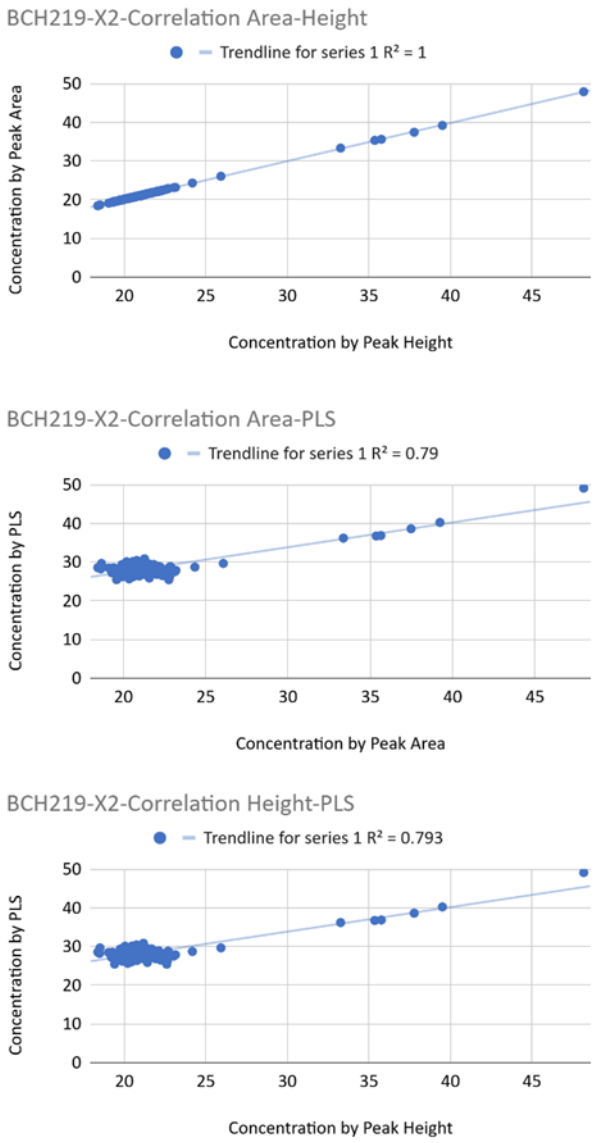

Figure 5.9. R^2 similarity correlation between peak area, peak height and the reduced range PLS model for 110°C, 5g.

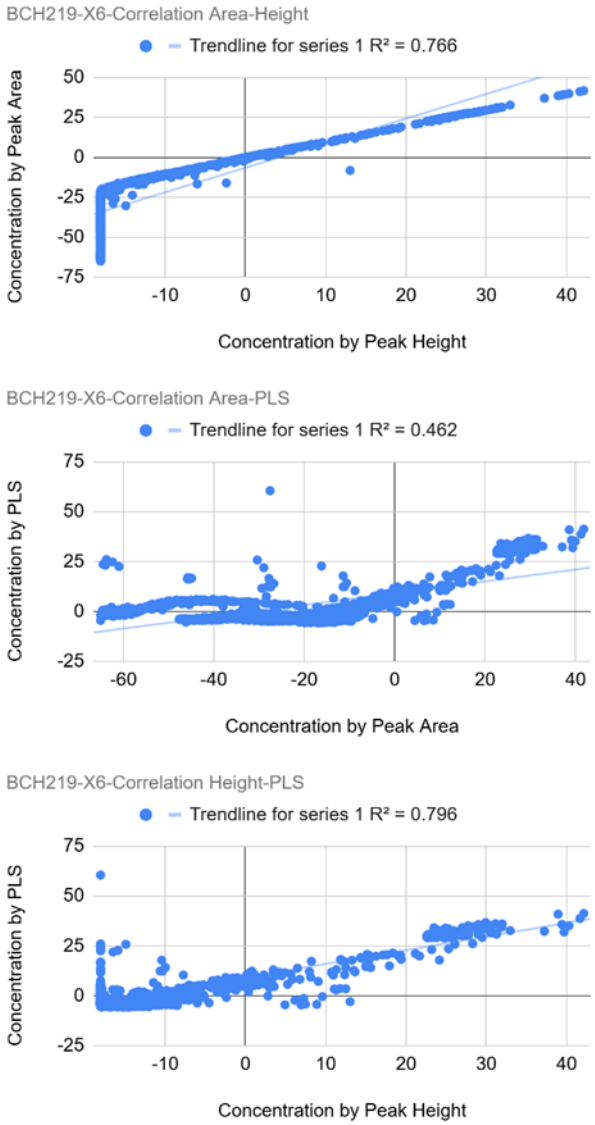

Figure 5.10. R^2 similarity correlation between peak area, peak height and the reduced range PLS model for 80°C, 20g.

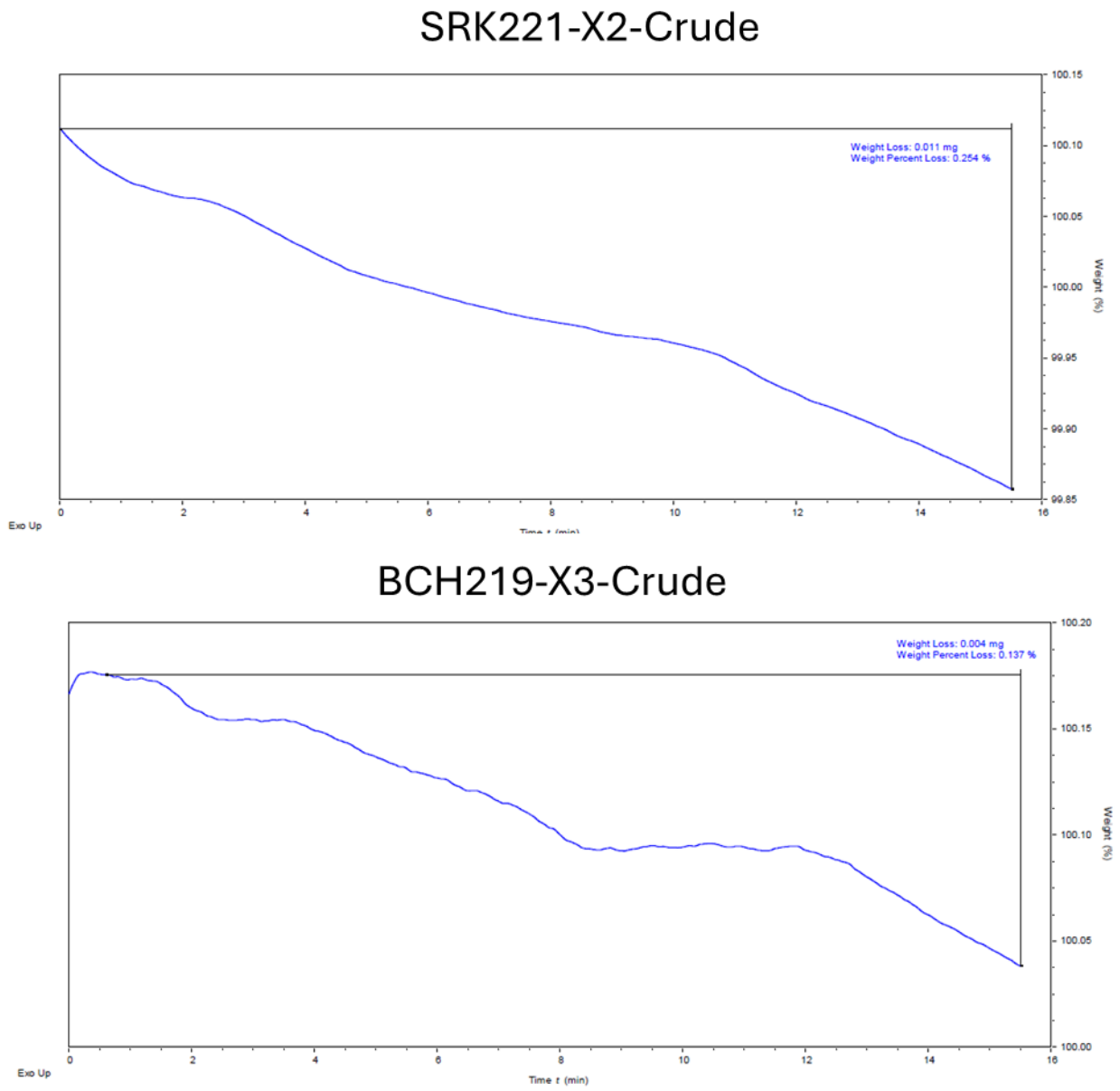

Figure 5.11. TGA thermogram showing mass/solvent loss of the final, isolated solid. Data is for the 60°C reactions.

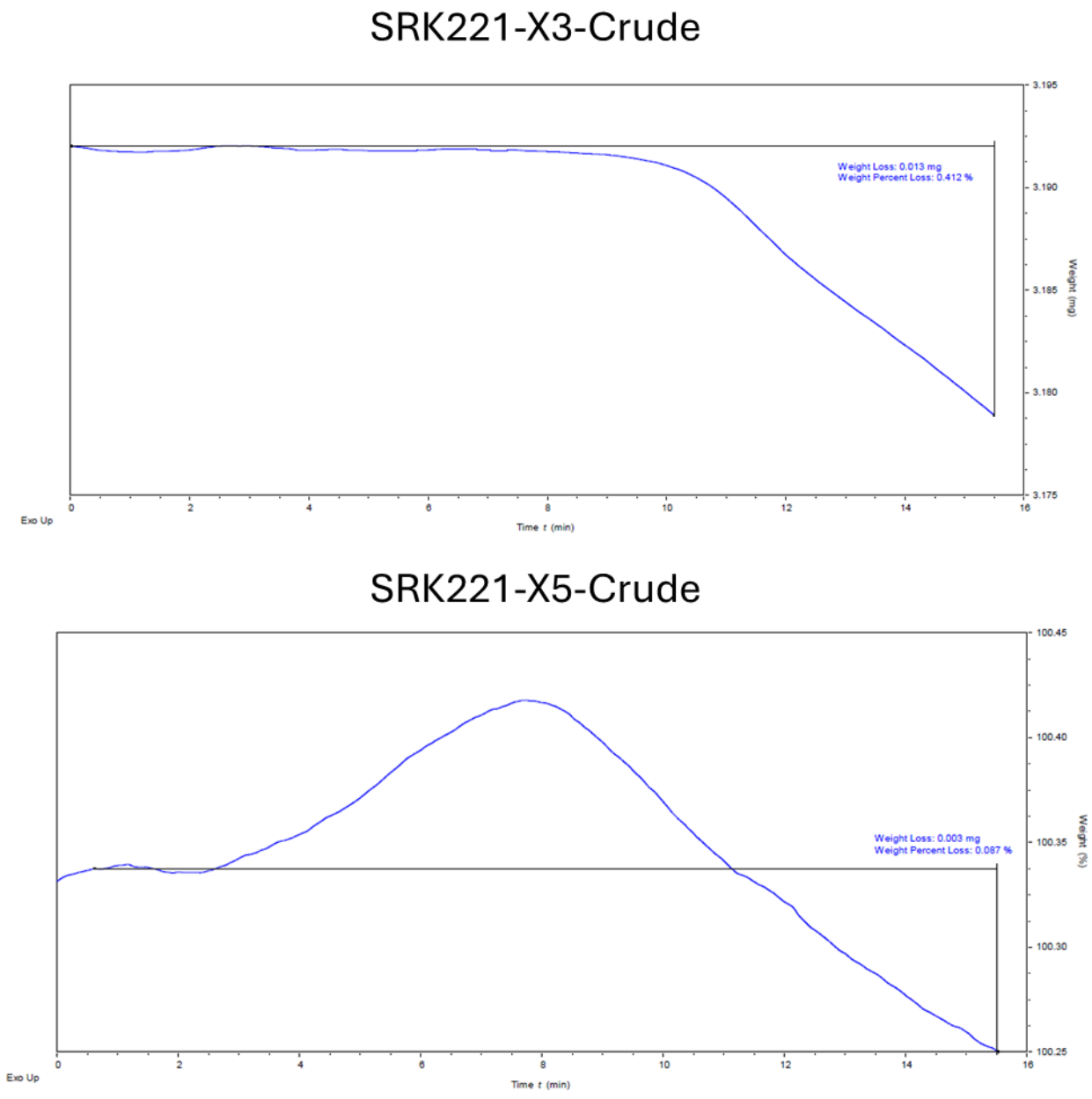

Figure 5.12. TGA thermogram showing mass/solvent loss of the final, isolated solid. Data is for the 80ºC reactions at 5 g.

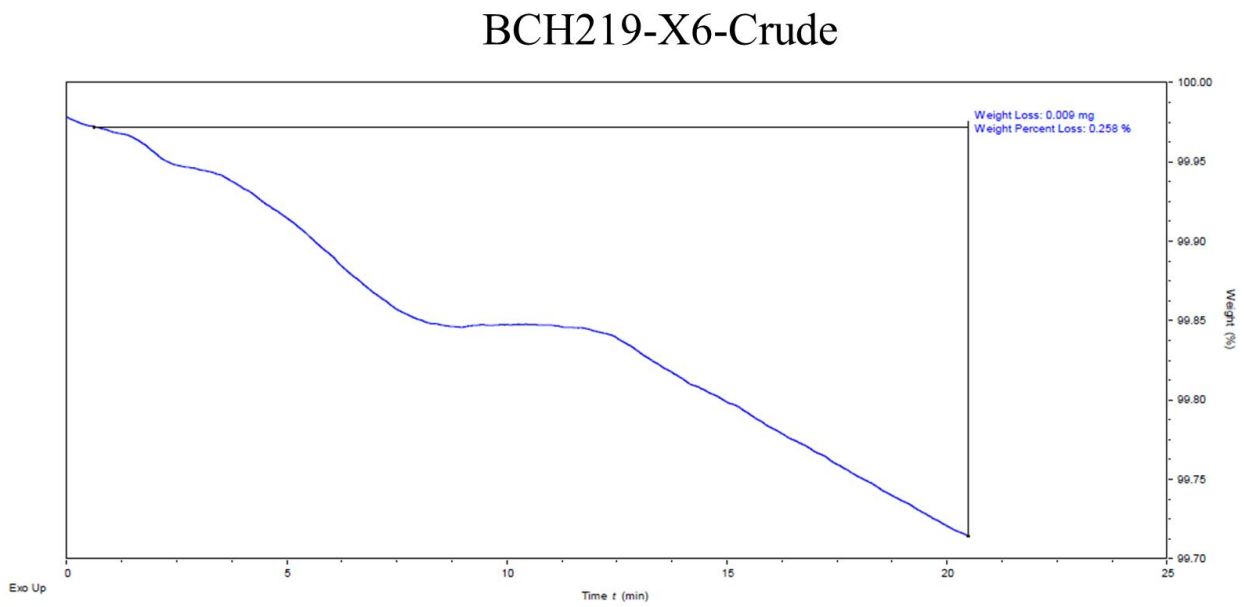

Figure 5.13. TGA thermogram showing mass/solvent loss of the final, isolated solid. Data is for the 80ºC reaction and 20g scale.

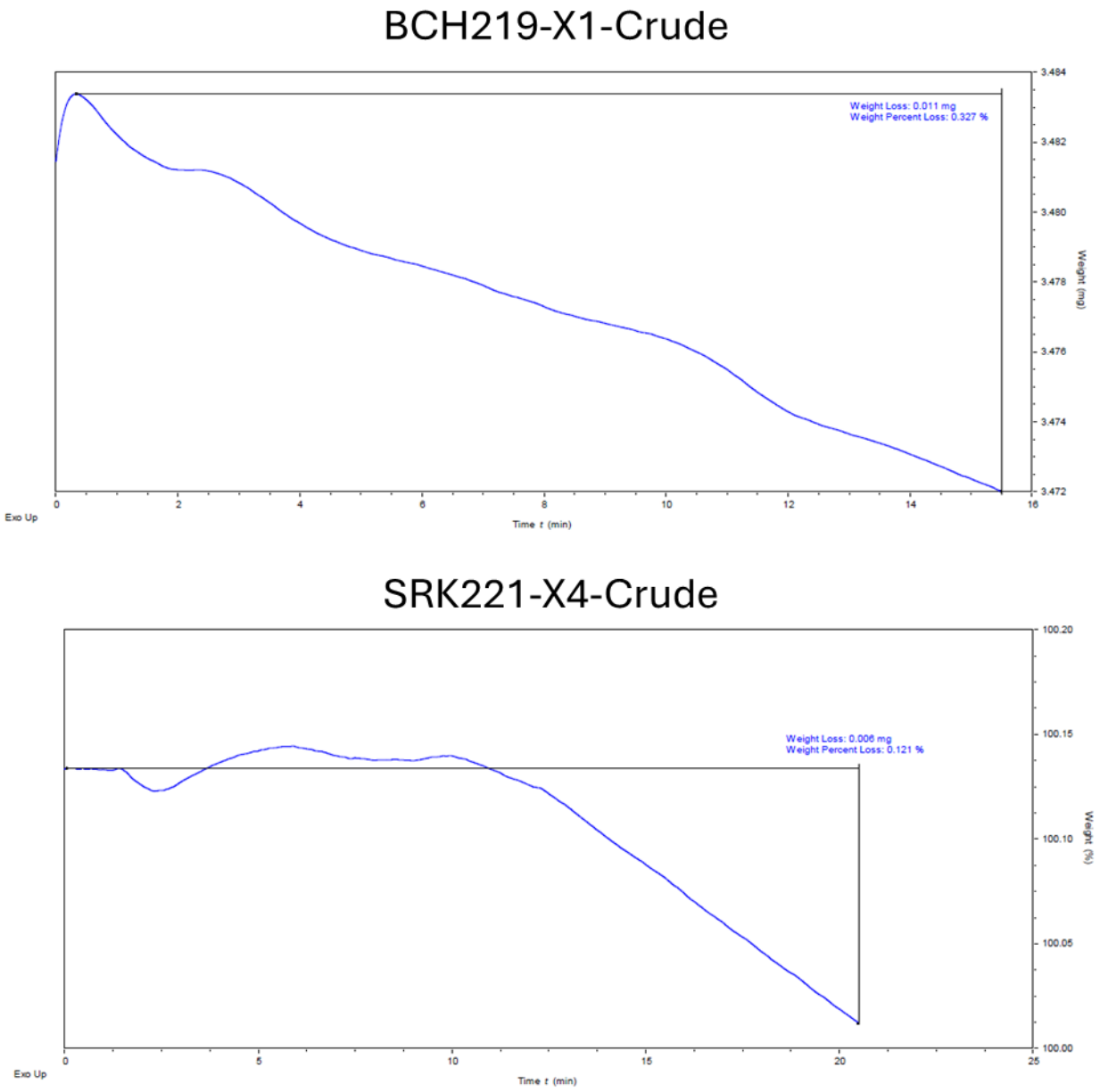

Figure 5.14. TGA thermogram showing mass/solvent loss of the final, isolated solid. Data is for the 100ºC reactions.

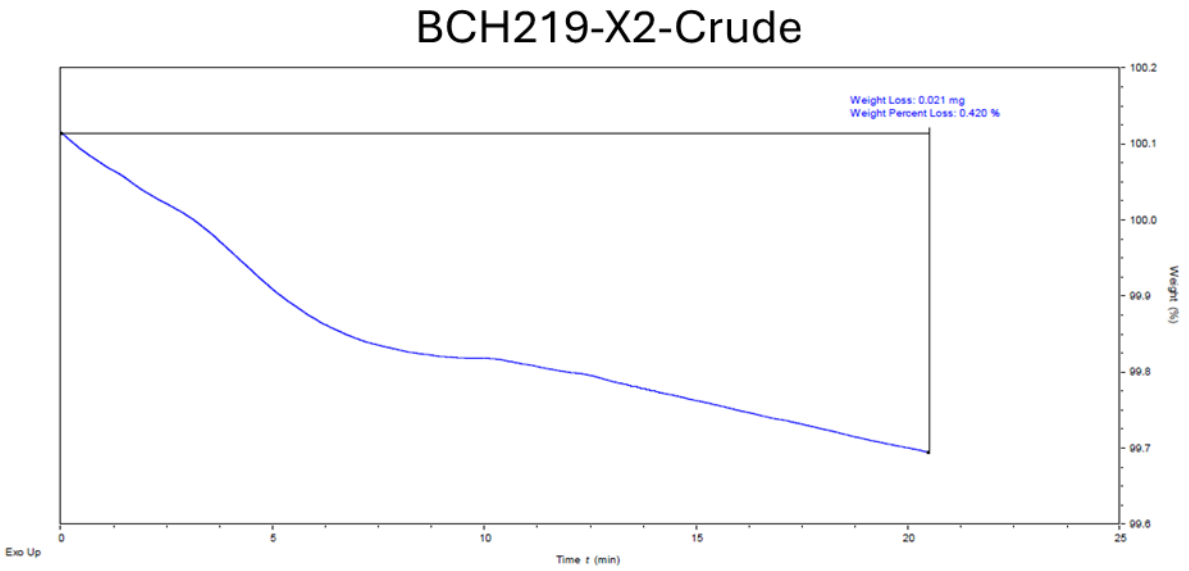

Figure 5.15. TGA thermogram showing mass/solvent loss of the final, isolated solid. Data is for the 110°C reaction.

6 Acknowledgements

This work was supported with funding from the Gates Foundation. M4ALL would like to express our gratitude to Dr. Trevor Laird, Dr. John Dillon, and Dr. Mark Krook for their helpful technical guidance, as well as Dr. John Walker and Mr. Scott Rosenblum for the ongoing collaboration and support of the M4ALL mission. The authors thank Dr. Saeed Ahmad and his team for their boundless efforts in TE analysis.

7 References

(1) Bester, S. M.; Wei, G.; Zhao, H.; Adu-Ampratwum, D.; Iqbal, N.; Courouble, V. V.; Francis, A. C.; Annamalai, A. S.; Singh, P. K.; Shkriabai, N.; Van Blerkom, P.; Morrison, J.; Poeschla, E. M.; Engelman, A. N.; Melikyan, G. B.; Griffin, P. R.; Fuchs, J. R.; Asturias, F. J.; Kvaratskhelia, M. Structural and Mechanistic Bases for a Potent HIV-1 Capsid Inhibitor. Science 2020, 370 (6514), 360–364. https://doi.org/10.1126/science.abb4808.

(2) Chun, H. M.; Dirlikov, E.; Cox, M. H.; Sherlock, M. W.; Obeng-Aduasare, Y.; Sato, K.; Voetsch, A. C.; Ater, A. D.; Romano, E. R.; Tomlinson, H.; Modi, S.; Achrekar, A.; Nkengasong, J.; CDC Global

HIV Working Group; CDC Global HIV Working Group; Agolory, S.; Amann, J.; Baack, B.; Behel, S.; Date, A.; Hanson, J.; Killam, W. P.; Patel, H.; Patel, S.; Pati, R.; Porter, L.; Warner, A.; Wuhib, T.; Zeh, C.; Faria E Silva Santelli, A. C.; Guevara, G.; Morales, R. E.; Ekra, A. K.; Kitenge, F.; Bonilla, L.; Mazibuko, S.; Damena, T.; Joseph, P.; Upadhyaya, S.; Aitmagambetova, I.; Mwangi, J.; Usmanova, N.; Xaymounvong, D.; Asiimwe, M.; Alice, M.; Masamha, G. J.; Mutandi, G.; Odafe, S.; Romel, L.; Musoni, C.; Mogashoa, M.; Bolo, A.; Nabidzhonov, A.; Mgomella, G.; Lolekha, R.; Alamo-Talisuna, S.; Podolchak, N.; Nguyen, C. K.; Quaye, S.; Mwila, A.; Nyika, P. Vital Signs : Progress Toward Eliminating HIV as a Global Public Health Threat Through Scale-Up of Antiretroviral Therapy and Health System Strengthening Supported by the U.S. President's Emergency Plan for AIDS Relief — Worldwide, 2004–2022. MMWR Morb. Mortal. Wkly. Rep. 2023, 72 (12), 317–324. https://doi.org/10.15585/mmwr.mm7212e1.

(3) Phillips, A. N.; Venter, F.; Havlir, D.; Pozniak, A.; Kuritzkes, D.; Wensing, A.; Lundgren, J. D.; Ee Luca, A.; Pillay, D.; Mellors, J.; Cambiano, V.; Bansi-Matharu, L.; Nakagawa, F.; Kalua, T.; Jahn, A.; Apollo, T.; Mugurungi, O.; Clayeen, P.; Gupta, R. K.; Barnabas, R.; Revill, P.; Cohn, J.; Bertagnolio, S.; Calmy, A. Risks and Benefits of Dolutegravir-Based Antiretroviral Drug Regimens in Sub-Saharan Africa: A Modeling Study. Lancet HIV 2019, 6 (2), e116–e127. https://doi.org/10.1016/S2352-3018(18)30317-5.

(4) Margot, N. A.; Naik, V.; VaneerVeen, L.; Anoshchenko, O.; Singh, R.; Dvory-Sobol, H.; Rhee, M. S.; Callebaut, C. Resistance Analyses in Highly Treatment-Experienced People With Human Immunodeficiency Virus (HIV) Treated With the Novel Capsid HIV Inhibitor Lenacapavir. J. Infect. Dis. 2022, 226 (11), 1985–1991. https://doi.org/10.1093/infdis/jiac364.

(5) Dvory-Sobol, H.; Shaik, N.; Callebaut, C.; Rhee, M. S. Lenacapavir: A First-in-Class HIV-1 Capsid Inhibitor. Curr. Opin. HIV AIDS 2022, 17 (1), 15–21. https://doi.org/10.1097/COH.0000000000000713.

(6) Zhang, J.-Y.; Wang, Y.-T.; Sun, L.; Wang, S.-Q.; Chen, Z.-S. Synthesis and Clinical Application of New Drugs Approved by FDA in 2022. Mol. Biomed. 2023, 4 (1), 26. https://doi.org/10.1186/s43556-023-00138-y.

(7) Zhuang, S.; Torbett, B. E. Interactions of HIV-1 Capsid with Host Factors and Their Implications for Developing Novel Therapeutics. Viruses 2021, 13 (3), 417. https://doi.org/10.3390/v13030417.

(8) Margot, N.; Ram, R.; Rhee, M.; Callebaut, C. Absence of Lenacapavir (GS-6207) Phenotypic Resistance in HIV Gag Cleavage Site Mutants and in Isolates with Resistance to Existing Drug Classes. Antimicrob. Agents Chemother. 2021, 65 (3), e02057-20. https://doi.org/10.1128/AAC.02057-20.

(9) Guinle, M. I. B. A New Way to Prevent HIV Delivers Dramatic Results in Trial. NPR. July 3, 2024. https://www.npr.org/sections/goats-and-soda/2024/07/03/g-s1-7988/hiv-prevention-drug-clinical-trial (accessed 2024-07-23).

(10) Gilead's Twice-Yearly Lenacapavir Demonstrated 100% Efficacy and Superiority to Daily Truvada® for HIV Prevention. https://www.gilead.com/news-and-press/press-room/press-releases/2024/6/gileads-twiceyearly-lenacapavir-eemonstrated-100-efficacy-and-superiority-to-daily-truvada-for-hiv-prevention (accessed 2024-07-23).

(11) Gilead to Highlight Landmark Progress in Research Across HIV Prevention, Treatment and Cure Programs at AIDS 2024. https://www.gilead.com/news-and-press/press-room/press-releases/2024/7/gilead-to-highlight-landmark-progress-in-research-across-hiv-prevention-treatment-and-cure-programs-at-aids-2024 (accessed 2024-07-23).

(12) Bauer, L. E.; Gorman, E. M.; Mulato, A. S.; Rhee, M. S.; Rowe, C. W.; Sellers, S. P.; Stefanidis, D.; Tse, W. C.; Yant, S. R.; Chiu, A. Capsid Inhibitors for the Treatment of Hiv. WO2020018459A1,

January 23, 2020. https://patents.google.com/patent/WO2020018459A1/en?oq=WO%C2%A02020018459 (accessed 2021-02-17).

(13) Allan, K. M.; Batten, A. L.; Brizgys, G.; Dhar, S.; Doxsee, I. J.; Goldberg, A.; Heumann, L. V.; Huang, Z.; Kadunce, N. T.; Kazerani, S.; Lew, W.; Ngo, V. X.; O'keefe, B. M.; Rainey, T. J.; Roberts, B. J.; Shi, B.; Steinhuebel, D. P.; Tse, W. C.; Wagner, A. M.; Wang, X.; Wolckenhauer, S. A.; Wong, C. Y.; Zhang, J. R. Methods and Intermediates for Preparing a Therapeutic Compound Useful in the Treatment of Retroviridae Viral Infection. WO2019161280A1, August 22, 2019.

(14) Link, J. O.; Rhee, M. S.; Tse, W. C.; Zheng, J.; Somoza, J. R.; Rowe, W.; Begley, R.; Chiu, A.; Mulato, A.; Hansen, D.; Singer, E.; Tsai, L. K.; Bam, R. A.; Chou, C.-H.; Canales, E.; Brizgys, G.; Zhang, J. R.; Li, J.; Graupe, M.; Morganelli, P.; Liu, Q.; Wu, Q.; Halcomb, R. L.; Saito, R. D.; Schroeeer, S. D.; Lazerwith, S. E.; Bondy, S.; Jin, D.; Hung, M.; Novikov, N.; Liu, X.; Villaseñor, A. G.; Cannizzaro, C. E.; Hu, E. Y.; Aneerson, R. L.; Appleby, T. C.; Lu, B.; Mwangi, J.; Liclican, A.; Niedziela-Majka, A.; Papalia, G. A.; Wong, M. H.; Leavitt, S. A.; Xu, Y.; Koditek, D.; Stepan, G. J.; Yu, H.; Pagratis, N.; Clancy, S.; Ahmadyar, S.; Cai, T. Z.; Sellers, S.; Wolckenhauer, S. A.; Ling, J.; Callebaut, C.; Margot, N.; Ram, R. R.; Liu, Y.-P.; Hyland, R.; Sinclair, G. I.; Ruane, P. J.; Crofoot, G. E.; McDonald, C. K.; Brainard, D. M.; Lad, L.; Swaminathan, S.; Sundquist, W. I.; Sakowicz, R.; Chester, A. E.; Lee, W. E.; Daar, E. S.; Yant, S. R.; Cihlar, T. Clinical Targeting of HIV Capsid Protein with a Long-Acting Small Molecule. Nature 2020, 584 (7822), 614–618. https://doi.org/10.1038/s41586-020-2443-1.

(15) Graupe, M.; Henry, S. J.; Link, J. O.; Rowe, C. W.; Saito, R. D.; Schroeeer, S. D.; Stefanidis, D.; Tse, W. C.; Zhang, J. R. Therapeutic Compounds Useful for the Prophylactic or Therapeutic Treatment of an Hiv Virus Infection. WO2018035359A1, February 22, 2018.

(16) Du, Z.; Farand, J.; Guney, T.; Kato, D.; Link, J. O.; Mack, J. B. C.; Mun, D. M.; Watkins, W. J.; Zhang, J. R. Therapeutic Compounds for HIV Virus Infection. WO2023102529A1, June 8, 2023.

(17) Brands, K. M. J.; Davies, A. J. Crystallization-Induced Diastereomer Transformations. Chem. Rev. 2006, 106 (7), 2711–2733. https://doi.org/10.1021/cr0406864.

(18) Medicines for All Institute (M4ALL), Process Development Report (PDR) for Synthesis of Frag A of Lenacapavir, 2024. https://medicines4all.vcu.edu/media/medicines4all/assets/documents/Len%20Frag%20A%20PDR.pdf.

(19) Schuurmans, J. H. A.; Zondag, S. D. A.; Chaudhuri, A.; van der Schaaf, J.; Noël, T. Stirring the Debate; How Mixing Influences Reproducibility and Efficiency in Synthetic Organic Chemistry. ACS Central Science https://doi.org/10.1021/acscentsci.5c01825 (accessed 2026-01-22).